# Solar wind turbulence and shear: A superposed-epoch analysis of corotating interaction regions at 1 AU

Joseph E. Borovsky[1] and Michael H. Denton[2]

Received 6 October 2009; revised 2 February 2010; accepted 29 March 2010; published 2 October 2010.

[1] A superposed-epoch analysis of ACE and OMNI2 measurements is performed on 27 corotating interaction regions (CIRs) in 2003–2008, with the zero epoch taken to be the stream interface as determined by the maximum of the plasma vorticity. When the measurements are rotated into the local-Parker-spiral coordinate system, the shear is seen to be abrupt. Converging flows are seen; about half of the CIRs show a layer of divergent rebound flow away from the stream interface. Analysis of the turbulence across the CIRs is performed. When possible, the effects of discontinuities are removed. Fluctuation amplitudes, the Alfvenicity, and the level of Alfvenic correlations all vary smoothly across the CIR. The Alfven ratio exhibits a decrease at the shear zone of the stream interface. Fourier analysis of subintervals is performed, and the results are superposed averaged as an ensemble of realizations. The spectral slopes of the velocity, magnetic field, and total energy vary smoothly across the CIR. The total-energy spectral index is ~3/2 in the slow and fast wind and in the CIRs. Fourier analysis of Elsasser fluctuations shows a smooth transition across the CIR from an inward-outward balance in the slow wind to an outward dominance in the fast wind. Spreading of turbulence away from the region where it is produced is limited to ~$10^6$ km. A number of signatures of turbulence driving at the shear zone are sought (entropy change, turbulence amplitude, Alfvenicity, spectral slopes, and in-out nature): none show evidence of driving of turbulence by shear.

**Citation:** Borovsky, J. E., and M. H. Denton (2010), Solar wind turbulence and shear: A superposed-epoch analysis of corotating interaction regions at 1 AU, *J. Geophys. Res.*, *115*, A10101, doi:10.1029/2009JA014966.

## 1. Introduction

[2] Turbulence in a magnetized plasma is characterized by a spectrum of velocity fluctuations and of magnetic field fluctuations that both have a large range of time scales and length scales. One famously turbulent plasma is the solar wind. With in situ spacecraft instrumentation, the solar wind provides a unique opportunity to study the physics of turbulence in magnetized collisionless plasmas [cf. *Veltri*, 1994; *Tu and Marsch*, 1995a; *Goldstein et al.*, 1995; *Goldstein and Roberts*, 1999; *Goldstein*, 2001; *Oughton*, 2003; *Smith*, 2003; *Bruno and Carbone*, 2005]. Extrapolations of solar wind measurements are regularly made to astrophysical turbulence [e.g., *Bhattacharjee et al.*, 1998; *Lithwick and Goldreich*, 2003; *Spangler and Spitler*, 2004]. Three major issues regarding turbulence in a collisionless plasma are (1) the driving (how the fluctuations arise), (2) the dynamics (the nature of the fluctuations and how they interact), and (3) the dissipation (what physical mechanisms dissipate the fluctuations and where the energy goes). This paper deals with the driving of turbulence in the collisionless solar wind plasma.

[3] For Navier-Stokes fluids, the driving of turbulence is not a mystery: typically shear in large-scale fluid motion powers the turbulent fluctuations in high-Reynolds-number flows [e.g., *Humphreys*, 1960; *Schlichting*, 1979; *Ashforth-Frost et al.*, 1997; *Pope*, 2000] (see also Appendix A). For collisionless plasmas, the driving of the turbulence is poorly understood [e.g., *Borovsky and Funsten*, 2003a; *Lucek et al.*, 2005; *Kuranz et al.*, 2005; *Schekochihin et al.*, 2007; *Cranmer*, 2008; *Mikhailovskii et al.*, 2008]. In computer simulations utilizing the MHD equations to describe magnetized plasmas, the turbulence is often driven by artificially pumping energy into a set of wave modes at large spatial scales [e.g., *Fyfe et al.*, 1977]; in other MHD computer simulations turbulence is driven by shearing a flow [*Mininni et al.*, 2005a]. A turbulent cascade of energy to shorter spatial scales can result. In the collisionless solar wind, the source of the turbulence is an outstanding issue [e.g., *Goldstein et al.*, 1995]. Arguments are that the energy for the turbulence resides in low-frequency large-amplitude outward traveling Alfven waves [*Bavassano and Bruno*, 1992; *Tu and Marsch*, 1995a; *Goldstein et al.*, 1999] or in the large velocity differences of differently moving parcels of plasma [*Coleman*, 1968; *Belcher and Davis*, 1971; *Roberts et al.*, 1992; *Goldstein et al.*, 1999]. The role of shearing of the low-frequency Alfven waves by large-scale plasma motions has also been invoked [*Roberts et al.*, 1987a, 1992; *Grappin and Velli*, 1996; *Ghosh et al.*, 1998; *Roberts and Ghosh*, 1999] as

[1]Los Alamos National Laboratory, Los Alamos, New Mexico, USA.
[2]Department of Physics, Lancaster University, Lancaster, UK.


0148-0227/10/2009JA014966

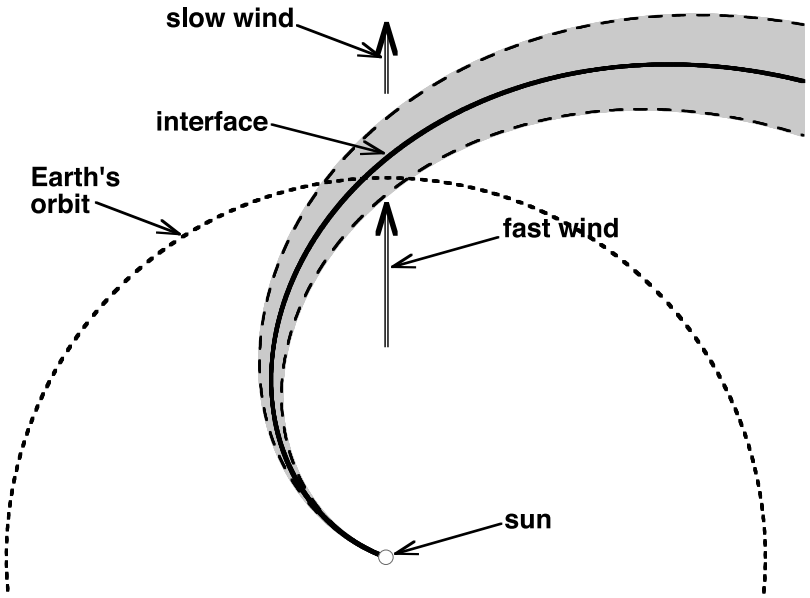


**Figure 1.** An idealized sketch of a corotating interaction region (CIR) in the equatorial plane. The CIR is shaded in gray with the stream interface denoted as the black curve.

has the reflection of outward traveling Alfven waves off structures in the plasma [*Bavassano and Bruno*, 1992; *Klein et al.*, 1993]. Through solar wind data analysis at 1 AU, this manuscript will investigate the relationships between turbulence and shear in the solar wind.

[4] This data-analysis study will focus on corotating interaction regions (CIRs) and the plasmas adjacent to them. Corotating interaction regions are grand, coherent, sheared flow structures [*Belcher and Davis*, 1971; *Gosling and Pizzo*, 1999; *Crooker and Gosling*, 1999; *Richardson*, 2006] that can be traced from near the Sun [*Richter and Luttrell*, 1986; *Tu et al.*, 1990] out to the orbit of Jupiter and beyond [*Gazis*, 1984; *González-Esparza and Smith*, 1997; *Siscoe and Intriligator*, 1993; *Lucek and Balogh*, 1998; *Intriligator et al.*, 2001]. Different regions of the solar surface produce wind with different speeds. CIRs are produced when the 27 day rotation of the Sun brings regions of the solar surface that produce fast solar wind into regions that were emitting slow wind (see Figure 1). As the radially outward flowing fast wind overtakes the radially outward flowing slow wind, an oblique region of compression and velocity shear results (gray shading in Figure 1). Beyond the CIR is slow solar wind: a plasma that is characterized by low specific entropy of ions. Along the center of the CIR is the stream interface, a boundary between slow and fast solar wind [*Gosling et al.*, 1978; *Forsyth and Marsch*, 1999]. Inside the CIR on the outward (from the Sun) side of the stream interface is compressed slow wind and inside the CIR on the inward (toward the Sun) side of the stream interface is compressed fast wind. On the near-Sun side of the CIR is fast solar wind: a plasma that is characterized by high specific entropy of ions. In the slow wind it has been argued that the turbulence is well developed, with fluctuations that propagate both inward and outward [*Tu et al.*, 1990; *Klein et al.*, 1993; *Bruno*, 1997; *Horbury and Schmidt*, 1999] [see also *Matthaeus et al.*, 1998]. In the fast wind it has been argued that the turbulence is young, with the fluctuations dominated by outward traveling Alfven waves [*Tu et al.*, 1990; *Horbury and Schmidt*, 1999].

[5] To complicate the picture of turbulence and shear in the solar wind, the solar wind plasma may not be homogeneous [cf. *Burlaga*, 1969; *Borovsky*, 2006]; rather it may be filled with fossil structure from the solar surface. At mesoscales (fractions of an AU) it contains "microstreams," which are regions wherein the flow velocity differs by ~50 km/s from its neighbors [*Neugebauer et al.*, 1995]. Microstreams have time scales (of convection past a satellite) of ~16 h [*Neugebauer et al.*, 1997]. It is argued that microstreams are unaltered from their creation at the solar surface [*Neugebauer et al.*, 1997]. At smaller scales (~1 h) the solar wind plasma may be parceled into flux tubes or flow tubes [*Parker*, 1963, 1964; *Ness et al.*, 1966; *McCracken and Ness*, 1966; *Bartley et al.*, 1966; *Mariani et al.*, 1973; *Thieme et al.*, 1988, 1989, 1990; *Tu and Marsch*, 1990, 1993; *Marsch*, 1991; *Bruno et al.*, 2001; *Borovsky*, 2008]. These tubes are characterized by large changes in the direction of the magnetic field, the plasma entropy and ionic composition, and the flow velocity. The walls of the tubes are characterized by tangential discontinuities [*Burlaga*, 1969; *Li*, 2007]. It is argued that the flux tubes form a braid about the Parker-spiral direction [*Bruno et al.*, 2001; *Borovsky*, 2008].

[6] This paper will present a thorough examination of the properties of solar wind turbulence relative to the strong shear zones of CIRs at 1 AU. Evidence for the driving of turbulence at the shear zones will be sought. Because of the repeatable features of CIRs in spacecraft data sets, superposed-epoch analysis will be performed. Earlier superposed-epoch studies of CIRs can be found in the work of *Gosling et al.* [1978], *Richter and Luttrell* [1986], and *McPherron and Weygand* [2006] [see also *Denton and Borovsky*, 2008, 2009; *Borovsky and Denton*, 2009].

[7] This manuscript is organized as follows. In section 2 the selection of the CIR events is explained, the data sets and data-analysis techniques are discussed, and a warning

**Table 1.** For the 27 Events Collected, the Time of Passage of the CIR Stream Interface Is Given for the L1 Point Upstream of the Earth

| Event | Year | Day of Year | UT, h | Evidence for Rebound[a] |
|---|---|---|---|---|
| 1 | 2003 | 125 | 1030 | no |
| 2 | 2003 | 233 | 0030 | no |
| 3 | 2003 | 260 | 0030 | no |
| 4 | 2004 | 43 | 0130 | no |
| 5 | 2005 | 2 | 0230 | yes |
| 6 | 2005 | 12 | 0330 | yes |
| 7 | 2005 | 38 | 1430 | yes |
| 8 | 2005 | 65 | 0730 | yes |
| 9 | 2005 | 227 | 1730 | no |
| 10 | 2005 | 306 | 1930 | yes |
| 11 | 2005 | 333 | 2130 | yes |
| 12 | 2005 | 361 | 1230 | yes |
| 13 | 2006 | 131 | 0130 | yes |
| 14 | 2006 | 165 | 2030 | no |
| 15 | 2006 | 267 | 0230 | yes |
| 16 | 2006 | 293 | 1830 | yes |
| 17 | 2006 | 327 | 0530 | yes |
| 18 | 2007 | 29 | 0930 | yes |
| 19 | 2007 | 117 | 1730 | no |
| 20 | 2007 | 138 | 0830 | no |
| 21 | 2007 | 345 | 0530 | no |
| 22 | 2008 | 5 | 0630 | no |
| 23 | 2008 | 41 | 0830 | no |
| 24 | 2008 | 86 | 1130 | yes |
| 25 | 2008 | 166 | 1630 | no |
| 26 | 2008 | 302 | 1930 | no |
| 27 | 2008 | 330 | 0430 | yes |

[a]Whether or not each CIR shows evidence of rebound (diverging flow) near the stream interface.

about the role of discontinuities in turbulence data analysis is given. In section 3 the structure of the CIRs are analyzed in particular by utilizing the local-Parker-spiral coordinate system wherein the vorticity is calculated. In section 4 the properties of the solar wind turbulence across the CIRs is analyzed, including fluctuation amplitudes, spectral indices, Alfven ratios, Alfvenicity, and inward-outward Elsasser fluctuations. In section 5 an argument is presented about the localization of any driven turbulence and the evidence for the driving of solar wind turbulence by shear in the CIRs is assessed. The findings of this study are summarized in section 6. In Appendix A, estimates are given of the scale sizes of turbulence driven in a shear and of the time required for the shear-driven turbulence cascade to fully develop.

## 2. Events, Data, and Turbulence

[8] For the superposed-epoch analysis of the solar wind and its turbulence at 1 AU, a set of 27 CIRs are collected. The CIR events are picked with three criteria: (1) that they have a clear, dominant shear zone as seen in the local-Parker-spiral coordinate system (see section 3), (2) that they do not contain interplanetary shocks, and (3) that they are followed by long (~ 3 days or more) intervals of high-speed (>600 km/s) wind. Some CIRs are characterized by multiple shear zones: those events were avoided. Using these three criteria, 27 events were selected in the years 2003–2008. These are listed in Table 1. For the superposed-epoch analysis, the zero epoch for the averaging was triggered on the maximum of the out-of-ecliptic-plane component of the vorticity in each CIR. The maximum of the CIR vorticity is the CIR stream interface (see section 3). For overviewing properties of the CIRs, the OMNI2 solar wind data set [*King and Papitashvili*, 2005] is used.

[9] Merged magnetic field and plasma measurements from the ACE spacecraft upstream from the Earth are used to analyze the MHD turbulence of the solar wind. The magnetic field measurements are from the MAG instrument [*Smith et al.*, 1998] and the plasma measurements are from the SWEPAM instrument [*McComas et al.*, 1998]. Fourier-transform techniques utilized are described in section 4.3 wherein spectral slopes are investigated.

[10] For some measures of the solar wind turbulence, strong discontinuities are removed from the data analysis. (Each time this is done, it is so noted.) The motivation for this removal is that discontinuities may be the walls of fossil flux tubes [*Burlaga*, 1968, 1969; *Borovsky*, 2008] [see also *Matthaeus et al.*, 2008], and these strong signals should be removed from the analysis of turbulence since they are not part of the turbulence. Tangential discontinuities (plasma boundaries) can have features attributable to turbulence and Alfven waves, such as (1) a spectral slope in the range of turbulence spectral slopes [*Siscoe et al.*, 1968; *Sari and Ness*, 1969], (2) high Alfvenicity [*Neugebauer et al.*, 1984, 1986; *Neugebauer*, 1985], and (3) a velocity and magnetic field perturbations consistent with outward propagation [*Neugebauer et al.*, 1984, 1986; *Neugebauer*, 1985]. Following *Borovsky* [2008], discontinuities are defined as changes in the direction of the magnetic field by more than 45° in two minutes or less or fractional changes in the vector velocity ($|\delta \mathbf{v}|/v$) that are 8.5% or more in two minutes or less. These values represent the positions of breakpoints in the occurrence distributions of the magnetic field direction changes and of $|\delta \mathbf{v}|/v$ (see, for instance, Figures 2 and 3 of *Borovsky* [2008]). The number density of discontinuities $N_d$ (number passed per hour and number per unit volume in the solar wind) is explored in section 3.

[11] An example of superposed-epoch analysis of the 27 CIR events appears in Figure 2. Data are averaged by adding all events together after they are shifted in time to a common trigger (the zero epoch). In the analysis of this paper, the common trigger is taken to be the CIR stream interface, as determined by the maximum in the vorticity in each CIR. In Figure 2 (top) the solar wind speed for the 27 individual CIR events is plotted as a function of time with time t = 0 (vertical dashed line) taken to be the passage of the stream interface. The plot extends from 5 days before the stream interface to 5 days afterward. In Figure 2 (middle) the average (mean value) solar wind speed of the 27 superposed

**Figure 2.** A superposed-epoch analysis of OMNI2 measurements of 27 CIRs, with the zero epoch taken as the time of stream-interface passage for each CIR. (top) The solar wind speed is plotted for each of the 27 CIRs. (middle) The superposed average of the solar wind speed is plotted (black curve). (bottom) The superposed average of the specific entropy of the solar wind ions is plotted (black curve). In Figure 2 (middle and bottom) the 25th and 75th percentiles of the specific entropy are plotted as red curves.

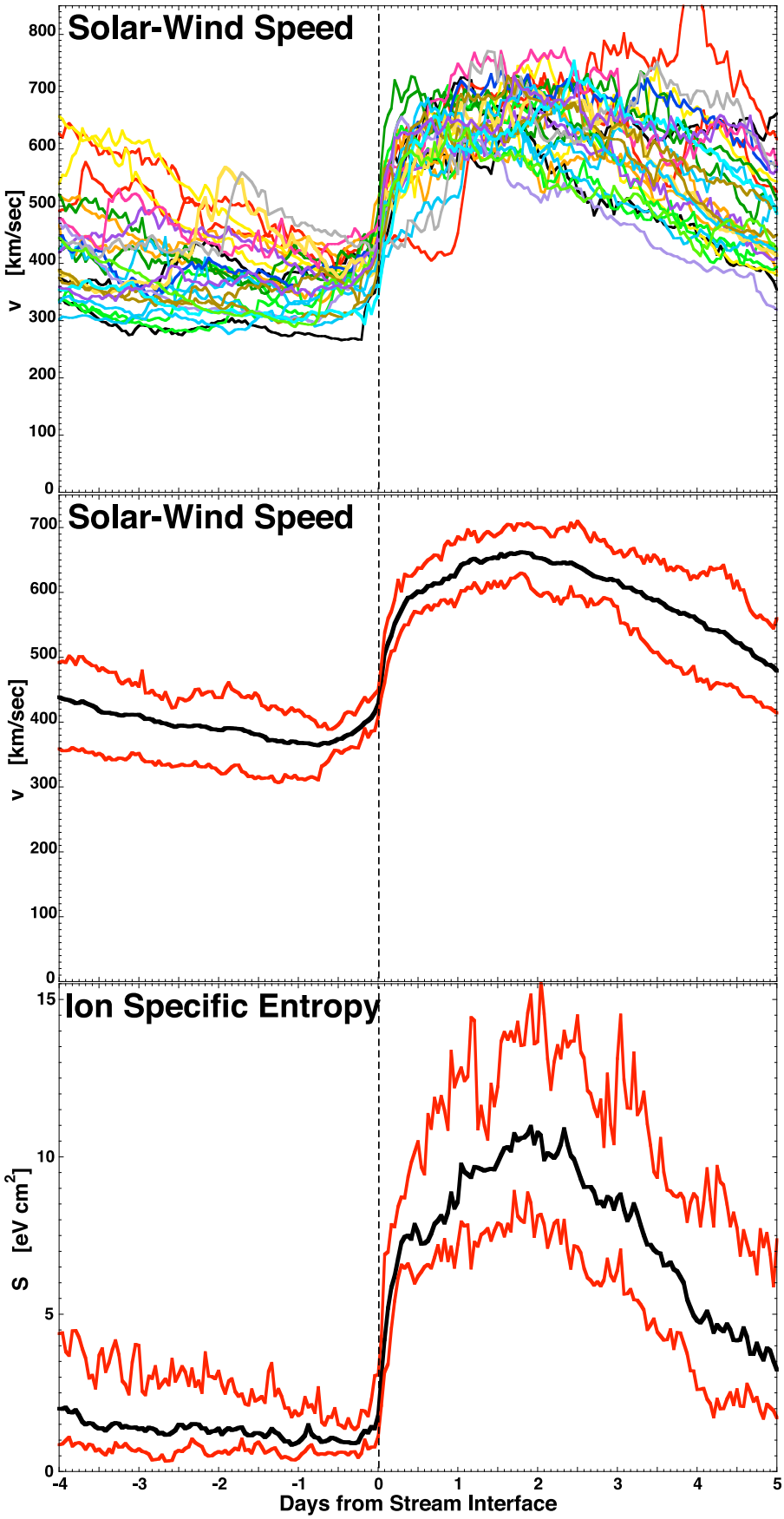
Solar-Wind Speed
v [km/sec]
Solar-Wind Speed
v [km/sec]
Ion Specific Entropy
S [eV cm$^2$]
Days from Stream Interface

**Figure 2**

events is plotted as the black curve, and the 25th and 75th percentiles of the speed are plotted as the red curves. Clearly the mean value in Figure 2 (middle) elucidates the trend underlying the 27 various events in Figure 2 (top): the wind is slow prior to the CIR passage, it rises through the CIR, and is fast afterward. (Note that how well the superposed average elucidates phenomena depends on the choice of the trigger [e.g., *Ilie et al.*, 2008; *Denton et al.*, 2010] as well as the selection of events.) In Figure 2 (bottom) the superposed average of the ion specific entropy $S = T_i/n^{2/3}$ for the 27 events is plotted (black curve) along with the 25th and 75th percentiles (red curves). Again, the superposed-epoch average illustrates the underlying trend: the specific entropy is low in the slow wind before the CIR passage, rises abruptly in the CIR, and is high in the fast wind after the CIR passage.

[12] As another example of superposed averaging, in Figure 3 the superposed-epoch averages of the solar wind speed and the ion specific entropy of the solar wind plasma are plotted for 35 days prior to the passage of the CIRs in Table 1 to 35 days afterward. Note the repeating of the signals on a 27 day cadence indicating the long duration of the CIRs. During the 2003–2008 era from which the CIR events were chosen, the pattern of coronal holes on the Sun tended to vary slowly and the Sun's rotation produces a corotating pattern with a 27 day periodicity to the wind speed (Figure 3, top) along with a 27 day periodicity in the type of plasma emitted at the Earth (Figure 3, bottom).

## 3. CIR Structure

[13] In this section the structure of CIRs as seen by superposed-epoch averaging triggered on the stream interface is examined. The more-standard properties of CIRs are overviewed in section 3.1 and vorticity and rebound (expanding) flows are examined in section 3.2.

### 3.1. Overview of CIR Structure

[14] In Figure 4 the averaged flow velocities and plasma parameters of the solar wind are plotted as a function of time for a superposition of the 27 CIRs of Table 1. The zero epoch is the CIR stream interface as determined by the maximum in the plasma vorticity (discussed below). The plots extend from 2 days prior to the passage of the stream interface (in the slow wind) to 3 days afterward (in the fast wind). The first panel of Figure 4 shows the rise in the solar wind speed associated with the passage of the CIR. In the second panel of Figure 4 the transverse component $v_t$ (in Rotational-Tangential-Normal RTN coordinates [cf. *Alevizos et al.*, 1999]) of the solar wind velocity is plotted. The characteristic east-west deflection in the CIR [*Siscoe et al.*, 1969; *Belcher and Davis*, 1971; *Richardson*, 2006] is evident in the plot, with the reversal in the sign of $v_t$ occurring very near the stream interface [*Gosling et al.*, 1978; *Richardson*, 2006; *McPherron and Weygand*, 2006]. In the third panel of Figure 4 the superposed averages of some of the basic properties of the solar wind plasma are plotted. Note the plasma number density n peaking very near the stream interface with the average number density n higher on the slow-wind side [see also *Gosling et al.*, 1978; *Richter and Luttrell*, 1986; *Richardson*, 2006]. The slow wind also contains noncompressive density enhancements associated with sector reversals upstream of the stream interface [*Gosling et al.*, 1981; *Borrini et al.*, 1981], making the slow-wind plasma lumpy. Note the average of the magnetic field strength B peaking near the stream interface with the field strength elevated on both sides of the interface [see also *Gosling et al.*, 1978; *Richter and Luttrell*, 1986; *Richardson*, 2006]. Note the ion temperature $T_i$ being low on the slow-wind side of the stream interface with an abrupt transition to high on the fast-wind side [cf. *Gosling et al.*, 1978]. (The electron temperature $T_e$ is not plotted here, but CIRs show elevated electron temperatures [cf. *Feldman et al.*, 1978; *Gosling et al.*, 1978].) Finally, in the third panel of Figure 4, note only a weak trend in the average of the alpha-to-proton ratio (in contrast to a stronger trend reported in the superposed-epoch analysis of *Gosling et al.* [1978]). In the fourth panel of Figure 4 the superposed averages of some characteristic speeds of the plasma are plotted: the Alfven speed $v_A = B/(4\pi n m_i)^{1/2}$, the ion thermal speed $v_{Ti} = (k_B T_i/m_i)^{1/2}$, the estimated ion-acoustic velocity $C_s = (k_B T_i + k_B T_e/m_i)^{1/2}$ (with $T_e$ taken to be 14.5 eV, which is close to the average value (14.7 eV) of ACE electron temperatures for the year 1998 when those temperatures were validated [cf. *Borovsky*, 2006; R. Skoug, private communication, 2009]), and the estimated magnetosonic speed $C_{ms} = (v_A^2 + C_s^2)^{1/2}$ which uses the estimate ion-acoustic speed. The general trend in the fourth panel of Figure 4 is that the characteristic speeds in the plasma tend to be higher in the fast wind after the passage of the CIR than they are in the slow wind ahead, with smooth transitions in the average speeds across the CIR from the slow wind to the fast wind. In the fifth panel of Figure 4 the superposed averages of the ion beta $\beta_i = 8\pi n k_B T_i/B^2$ and of the ion specific entropy $S = T_i/n^{2/3}$ are plotted. (In this panel, since ratios are being analyzed, logarithmic averaging is performed to keep less-than-unity values from being outweighed by greater-than-unity values.) The ion beta is somewhat higher in the slow wind than it is in the fast wind, with the averages of $\beta_i$ in both plasmas being greater than unity. Note that the total plasma beta (ion plus electron) is higher than $\beta_i$. The superposed average of the ion specific entropy is low in the slow wind and increases by almost tenfold in going from the slow wind to the fast wind [see also *Burlaga et al.*, 1990; *Siscoe and Intriligator*, 1993; *Lazarus et al.*, 2003].

[15] This overview of CIR structure at 1 AU is sketched in Figure 5, where a segment of a CIR is shown (shaded region) with the temporal track of a spacecraft across the CIR denoted as the dashed arrow pointing downward. The flow directions of the solar wind plasma in the Sun's reference frame in RTN coordinates are shown as the bold arrows. The flow is radially out from the Sun in the slow wind ahead of the CIR and in the fast wind behind the CIR. Within the CIR the flow is deflected. A spacecraft first sees the westward deflection of compressed slow wind and then sees the eastward deflection of the compressed fast wind, with the east-west flow reversal occurring at the stream interface. Some of the plasma properties of the slow and fast wind (a la Figure 4) are summarized in Figure 5.

### 3.2. Local-Parker-Spiral Coordinates, Vorticity, and Rebound

[16] CIRs are taken to be long-lived structures [*Burlaga and Lepping*, 1977; *Siscoe and Intriligator*, 1993; *McPherron and Weygand*, 2006] oriented along the Parker-spiral direction [cf. *Richardson*, 2006]. To estimate the vorticity $\underline{\omega} = \nabla \times \underline{v}$

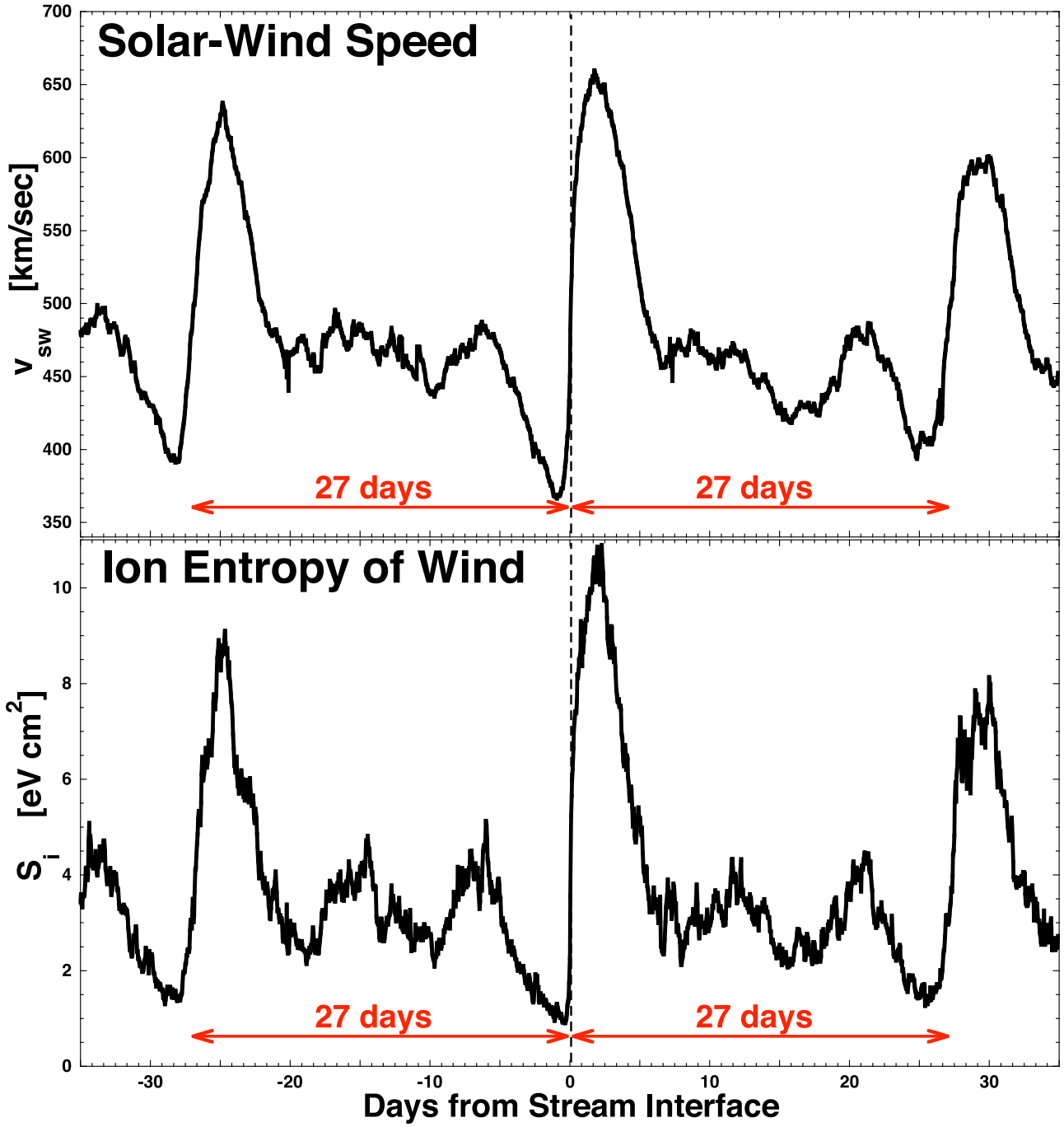


**Figure 3.** A superposed-epoch analysis of OMNI2 measurements for 27 CIRs, with the zero epoch taken to be the passage of the stream interface of each CIR. (top) The superposed average of the solar wind speed is plotted with the 27 day repetition of the solar wind speed clearly seen. (bottom) The superposed average of the specific ion entropy of the solar wind plasma is plotted with the 27 day repetition of the type of plasma emitted from the Sun clearly seen.

**Figure 4.** Superposed averages of OMNI2 measurements for the 27 CIR events of Table 1 are plotted. The zero epoch (vertical dashed line) is the passage of the stream interface. The first panel is the plot of the solar wind speed; the second panel is the plot of the transverse velocity of the solar wind; the third panel is the plot of the plasma number density, ion temperature, alpha-to-proton ratio, and magnetic field strength; the fourth panel is the plot of the Alfven speed, ion thermal speed, ion-acoustic speed, and magnetosonic speed; and the fifth panel is the plot of the ion specific entropy and the ion beta of the solar wind plasma. (To obtain the ion-acoustic and magnetosonic speeds, the electron temperature of the solar wind was taken to be 15 eV.)

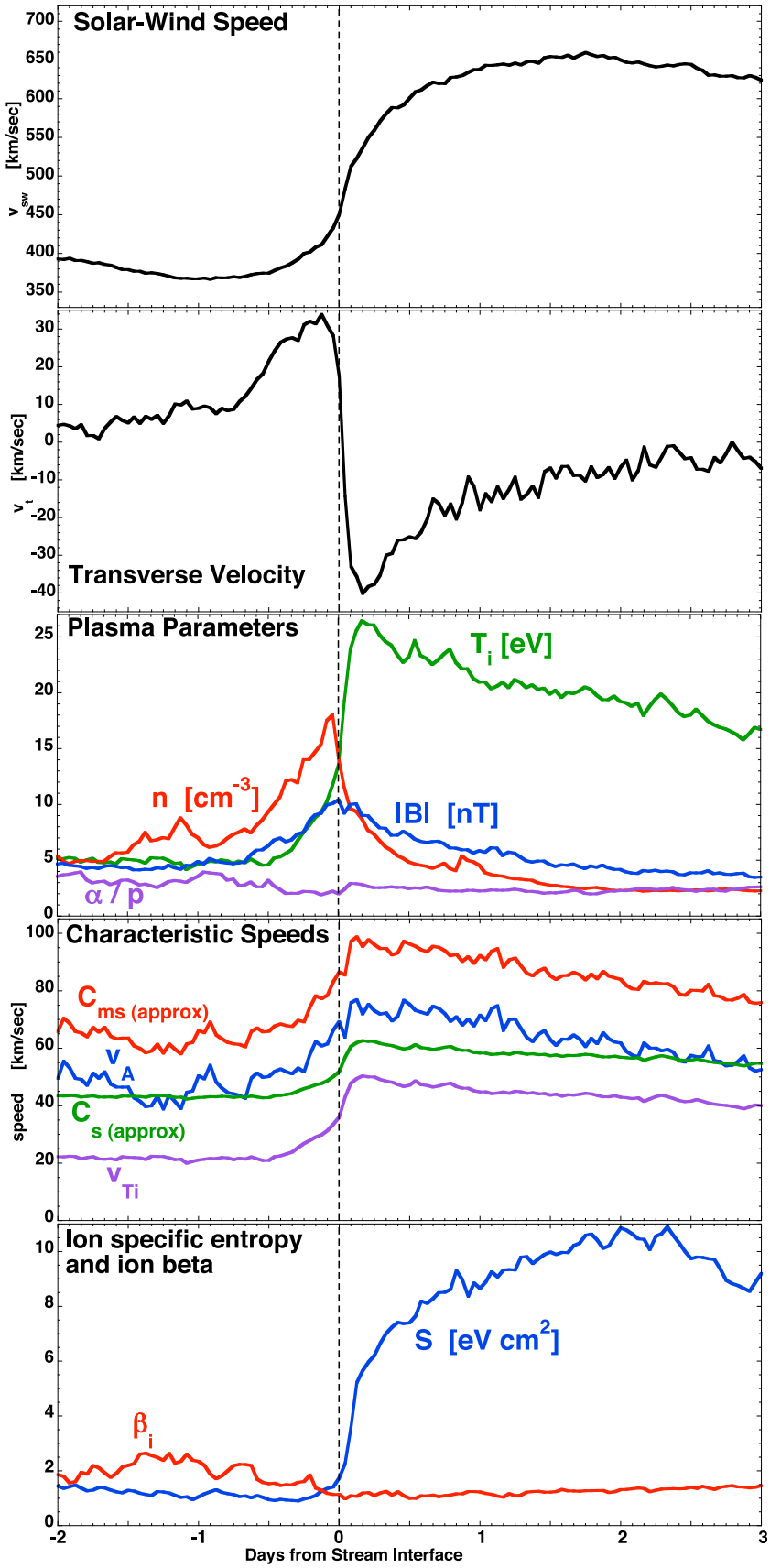
Solar-Wind Speed
$v_{sw}$ [km/sec]
Transverse Velocity
$v_t$ [km/sec]
Plasma Parameters
$T_i$ [eV]
n [cm$^{-3}$]
|B| [nT]
α / p
Characteristic Speeds
speed [km/sec]
$C_{ms\ (approx)}$
$v_A$
$C_{s\ (approx)}$
$v_{Ti}$
Ion specific entropy and ion beta
S [eV cm$^2$]
$\beta_i$
Days from Stream Interface

**Figure 4**

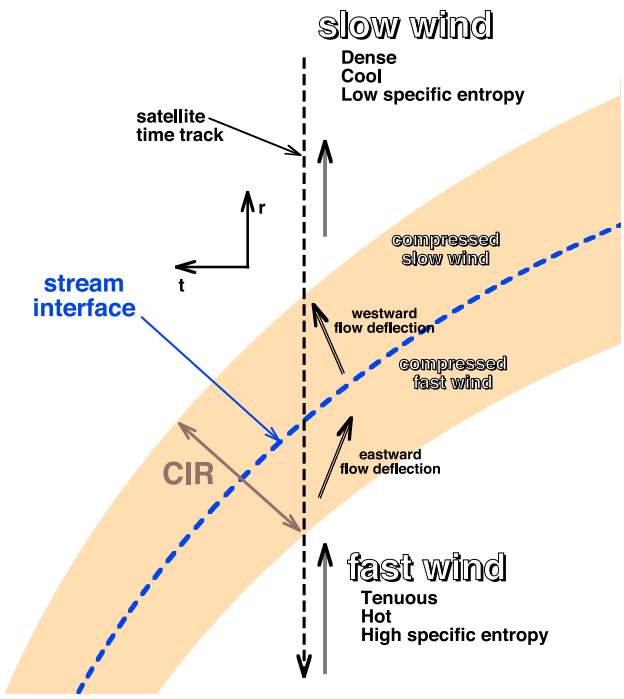


**Figure 5.** A sketch of a CIR in the vicinity of 1 AU. Standard view in the reference frame of the Sun in RTN coordinates. The reference frame emphasizes the westward-eastward flow deflection (arrows) in the CIR (brown shading).

in the solar wind plasma, (1) the CIR will be assumed to be a static pattern corotating with the Sun [*Pizzo*, 1978; *Gosling and Pizzo*, 1999] and (2) the flow measurements from spacecraft will be rotated into a "local-Parker-spiral" coordinate system. The directions "parallel" and "perpendicular" are denoted as in the direction of the Parker spiral and transverse to the direction of the Parker spiral in the ecliptic plane, respectively. In rotating from RTN to Parker-spiral coordinates, the rotation angle is given by the Parker-spiral winding angle from radial $\theta = \arctan(405/v_{sw})$, where $v_{sw}$ is the solar wind speed in km/s.

[17] The superposed-epoch average of the direction of the measured magnetic field direction relative to the predicted Parker-spiral direction is plotted in Figure 6. The thin curve has a resolution of 1 h and the thick curve is a running 13 h average of the black curve. Although it is well known that the instantaneous field has a large spread in values about the Parker-spiral direction [*Ness and Wilcox*, 1966; *Burlaga and Ness*, 1997; *Borovsky*, 2010], Figure 6 demonstrates that on average the magnetic field in the CIR systematically follows the local-Parker-spiral direction. Note that Figure 6 shows no clear evidence at 1 AU for underwinding (positive values) in the rarefaction region in the days prior to the CIR [cf. *Jones et al.*, 1998; *Murphy et al.*, 2002; *Riley and Gosling*, 2007].

[18] For two CIR events (events 10 and 27 in Table 1), the transformation from RTN to local-Parker-spiral coordinates is shown in Figure 7. In Figures 7a and 7b, the RTN radial and transverse velocities of the solar wind at 1 AU are plotted in black, and the parallel and perpendicular (to the Parker spiral) velocities of the solar wind are plotted in red. The vorticity $\partial v_{\parallel}/\partial x_{\perp}$ in the local-Parker-spiral coordinate system is plotted in Figures 7e and 7f, where $\partial v_{\parallel}/\partial x_{\perp} = (v_{sw} \sin\theta)^{-1} \partial v_{\parallel}/\partial t_{\perp}$ with the time derivative $\partial v_{\parallel}/\partial t_{\perp}$ obtained from the time series of solar wind measurements from a satellite. For these two CIRs, values of $\omega$ of $\sim 5 \times 10^{-5}$ s$^{-1}$ are obtained, similar to the values previously obtained for plasma slip zones in CIRs [*Borovsky*, 2006]. As can be seen in Figures 7a, 7b, 7e, and 7f, the shear in the CIR is abrupt rather than distributed [see also *Borovsky*, 2006]. In Figures 7b, 7d, and 7f the width of the shear zone (as determined by the vorticity) at the 2 November stream interface is much narrower than the width of the CIR (as determined by the width of the magnetic field compression region or the width of the region over which the solar wind speed changes). In Figures 7c and 7d the perpendicular (to the CIR) flow is plotted. Away from the stream interface itself the convergent flow toward the stream interface is clearly seen: positive flow before the CIR and negative flow afterward [see also *Hundhausen*, 1973; *Borovsky*, 2006].

[19] In Figure 8 the CIR morphology is sketched in the reference frame moving with the stream interface (which moves radially outward with the plasma at about 400 km/s). Also shown in Figure 8 is the Parker-spiral coordinate system. In the reference frame of the stream interface there is a convergent flow toward the stream interface from both the slow wind and the fast wind (in the perpendicular direction). Within the CIR there is a sheared flow with the compressed slow wind moving along the Parker spiral in the direction toward the Sun and the compressed fast wind moving along the Parker spiral in the direction away from the Sun. At the stream interface there is a large localized vorticity (an abrupt shear). The compressed slow and fast winds within the CIR also have compressional flows toward the stream interface perpendicular to the Parker spiral. In Figure 8 some of the important properties of the slow and fast wind are noted.

[20] Note in the right column of Figure 7 that there is a reversal in the $v_{\perp}$ flow around the stream interface itself: negative flow to the left and positive flow to the right. This represents divergent flow away from the stream interface. This is evidence for a rebound to the flow compression of the CIR. This rebound (diverging flow) around the stream interface, which is clear in the local-Parker-spiral coordinate system (red curves), is difficult to see in RTN coordinates (black curves). Of the 27 CIR events selected (see Table 1), 14 show evidence for such rebound in the vicinity of the steam interface. The rebound in the CIRs is explored further in Figure 9 where a superposed-epoch analysis is shown for the 14 CIRs that show evidence of rebound. For each of the CIR events a radial velocity equal to the radial velocity of the plasma at the time of passage of the stream interface is subtracted and then the velocity vector is rotated into the local-Parker-spiral coordinate system. In the first panel of Figure 9 the superposed average of the RTN transverse flow velocity $v_t$ is plotted and the region of east-west flow deflection (the boundaries of the CIR) are indicated by vertical dashed lines. Note in the second panel of Figure 9

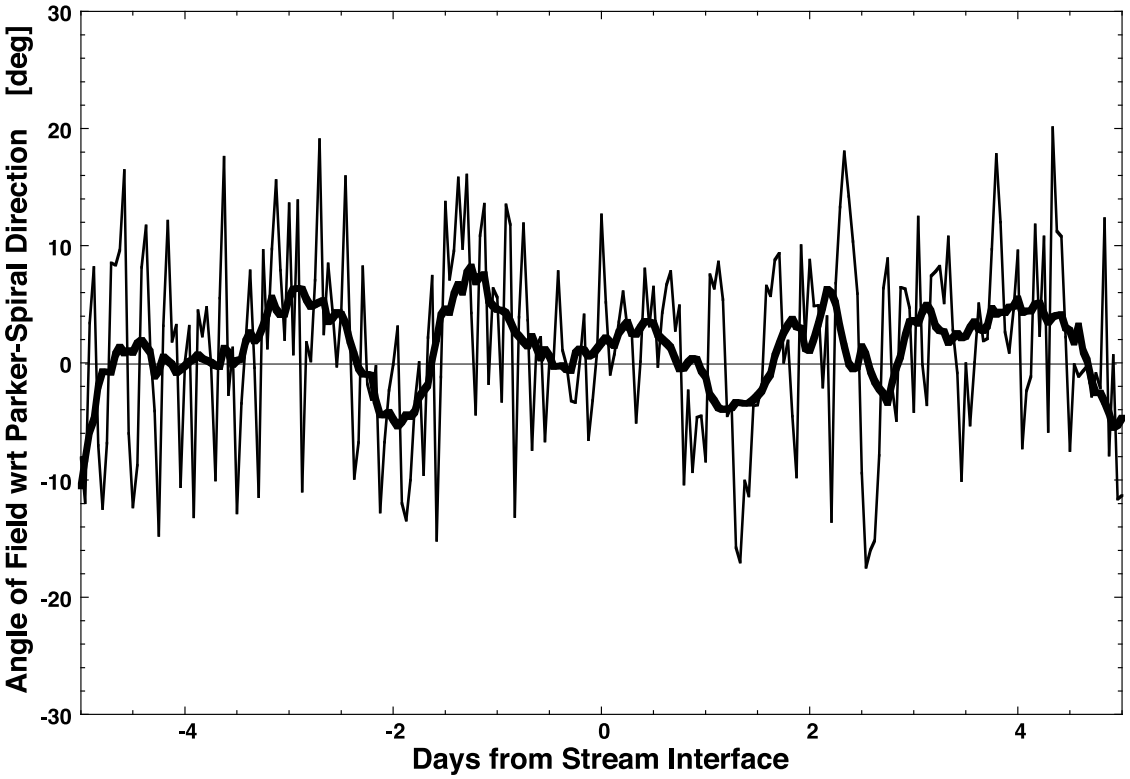


**Figure 6.** Using OMNI2 measurements, the superposed average of the difference between the direction of the projection of the measured magnetic field onto the solar-equatorial plane and the direction of the predicted Parker-spiral direction. Positive values are more radial than Parker spiral, and negative vales are more wound than Parker spiral. The small values of the average difference indicate that the magnetic field within the CIRs follows the local-Parker-spiral direction.

that the convergent $v_\perp$ flows are constant outside the CIR boundaries and decrease in magnitude within the CIR as the enhanced pressure in the compressed CIR slows the inflow. In the second panel of Figure 9 the superposed average of the flow perpendicular to the local-Parker-spiral direction is plotted and the region of rebound (divergent flow) is demarcated by vertical dashed lines. In the fourth panel of Figure 9 the superposed average of the vorticity $\omega = \partial v_{\|}/\partial x_\perp$ is plotted: the peak in the vorticity (identified as the CIR stream interface) is denoted by a vertical dashed line. In the third panel of Figure 9 the superposed average of the specific entropy $S = T_i/n^{2/3}$ of the plasma ions is plotted. Note that the specific entropy is constant on the slow-wind side of the stream interface and begins to abruptly increase when the stream interface passes.

## 4. Turbulence in CIRs and in the Slow and High-Speed Wind

[21] In this section the properties of the turbulent fluctuations of the solar wind are systematically analyzed across CIRs with the use of superposed-epoch averaging using the 27 CIRs of Table 1. The emphasis of the present investigation is to look for changes in the properties of the turbulence associated with velocity shear (vorticity) in the solar wind. The properties examined are the number density of discontinuities in the plasma (section 4.1), the amplitudes of turbulent fluctuations with and without discontinuities in the measurements (section 4.2), the Alfven ratio of the fluctuations (section 4.2) the Alfvenicity and the degree of Alfvenic correlation (section 4.3), the spectral indices of the velocity, magnetic field, and total energy (section 4.4), and the amplitudes and spectral indices of Elsasser-variable fluctuations (section 4.5). Previous less thorough analyses of solar wind turbulence across CIRs at various distances from the Sun can be found in the literature [e.g., *Belcher and Davis*, 1971; *Gosling et al.*, 1978; *Tu et al.*, 1990; *Grappin et al.*, 1990; *Lucek and Balogh*, 1998; *Crooker and Gosling*, 1999; *Horbury and Schmidt*, 1999; *Gulamali and Cargill*, 2001; *Intriligator et al.*, 2001; *Borovsky and Steinberg*, 2006a]; one previous analyses of solar wind turbulence across CIRs specifically utilized superposed-epoch techniques [*Gosling et al.*, 1978].

**Figure 7.** For two CIR events from Table 1 (event 10 without a rebound in the left column and event 27 with a rebound in the right column), (a, b) the RTN r and t velocities are plotted (black curves), (c, d) the local-Parker-spiral parallel and perpendicular velocities are plotted (red curves), and (e, f) the plasma vorticity is plotted. The vertical dashed lines are the times of passage of the stream interfaces.

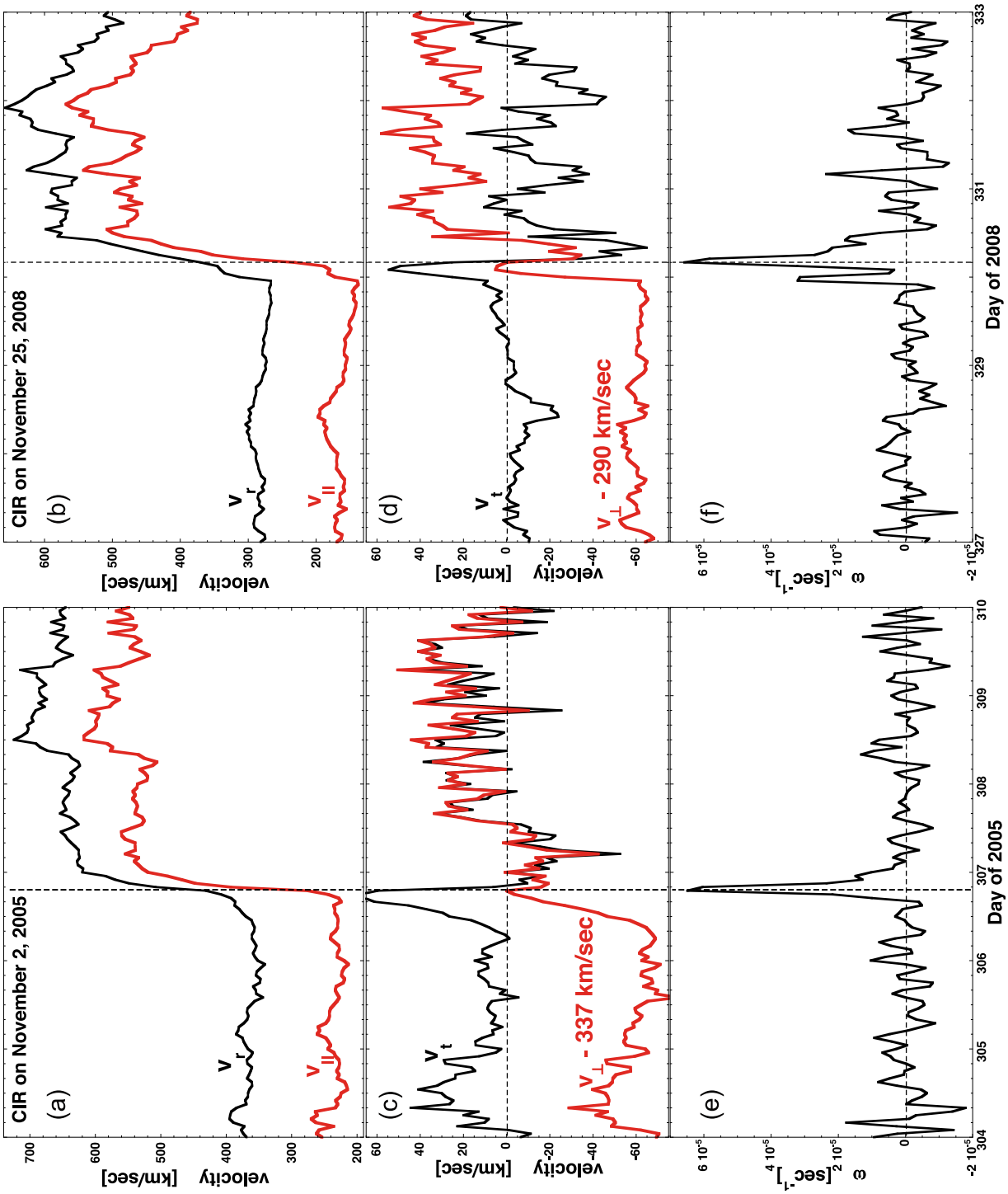
CIR on November 2, 2005
CIR on November 25, 2008
(a)
(b)
(c)
(d)
(e)
(f)
velocity [km/sec]
ω [sec⁻¹]
v_r
v_∥
v_t
v_⊥ - 337 km/sec
v_⊥ - 290 km/sec
Day of 2005
Day of 2008

Figure 7

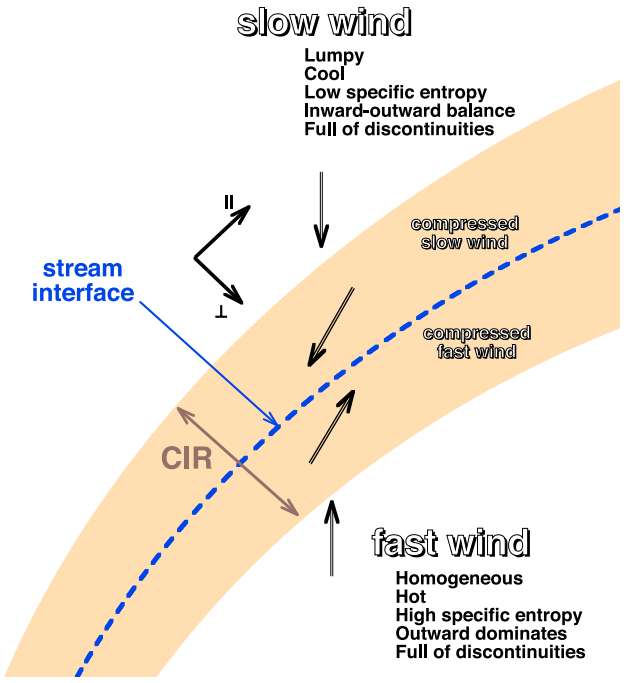


**Figure 8.** A CIR in the vicinity of 1 AU is sketched in the reference frame of the stream interface in the local-Parker-spiral coordinate system. This view emphasizes the shear (parallel to the Parker-spiral direction) and compression (perpendicular to the Parker-spiral direction). Here the steam interface is an abrupt shear zone with large localized vorticity that separates fast-wind plasma from slow-wind plasma.

### 4.1. Density of Discontinuities

[22] In Figure 10 (top) the superposed-epoch average of the number of discontinuities $N_d$ encountered per hour by the ACE spacecraft at 1 AU is plotted as a function of time with the zero epoch being the passage of the stream interface. The thin curve is the hourly averaged value and the thick curve is a 13 h running average. As stated in section 2, discontinuities are taken to be changes in the direction of the magnetic field by more than 45° in two minutes or less or fractional changes in the vector velocity ($|\delta \mathbf{v}|/v$) that are 8.5% or more in two minutes or less. As can be seen in Figure 10, more than one strong discontinuity is observed per hour on average in the solar wind before, after, and during CIRs. The discontinuity encounter rate is lower in the slow wind before CIRs than it is in the fast wind [see also *Tsurutani et al.*, 1994; *Tsurutani and Ho*, 1999; *Crooker and Gosling*, 1999; *Li*, 2007]. However, the encounter rate depends on the solar wind velocity (how much wind sweeps by the observing spacecraft) and the orientation of the magnetic field. In Figure 10 (bottom) the number density of discontinuities is plotted, assuming that the discontinuities are aligned with the Parker-spiral direction (as was shown by *Burlaga* [1969] and *Borovsky* [2008]). The number density of discontinuities (number of discontinuities per km) is given by $N_d^* = N_d/v_{sw}/\sin\theta$ were $\theta$ is the Parker-spiral orientation from radial $\theta = \arctan(405/v_{sw})$ and $N_d$ is the number of discontinuities seen per unit time on a spacecraft as the solar wind sweeps by with velocity $v_{sw}$. As can be seen in Figure 10 (bottom), the number density of discontinuities $N_d^*$ is somewhat higher in the fast wind after the CIR passage than it is in the slow wind before the CIR passage, and there is a local maximum of the number density $N_d^*$ in the compressed-fast-wind portion of the CIR.

### 4.2. Turbulence Amplitudes and the Alfven Ratio

[23] In Figure 11 the superposed averages of the amplitude of the velocity and magnetic field fluctuations in the solar wind as measured by ACE at 1 AU are plotted for the 27 CIR events of Table 1. In the first panel of Figure 11 the superposed average of the tangential flow velocity $v_t$ of the solar wind is plotted. From this $v_t$ curve, the outer boundaries of the CIR are denoted as dashed vertical lines. The central vertical dashed line marks the position of the stream interface as determined by the maximum in the plasma vorticity, which is plotted in the second panel of Figure 11. In the third panel of Figure 11 the amplitudes of the vector velocity fluctuations $\delta v$ and the vector magnetic field fluctuations $\delta \underline{B}$ are plotted. Two pairs of curves are plotted: the level of fluctuations including discontinuities (dashed curves) and the level of fluctuations excluding discontinuities (solid curves). If strong discontinuities are fossil structure in the solar wind and not part of the turbulence [e.g., *Borovsky*, 2008], then their presence will add errors to measurements of the amplitude of the turbulence; if this is the case then levels of fluctuations without discontinuities should be considered to be truer measures of the amplitude of the MHD turbulence in the solar wind. The amplitudes pertain to fluctuations with periods less than 7 min: the standard deviation $\delta v$ of $|\underline{v} - <\underline{v}>_7|$ and the standard deviation $\delta B$ of $|\underline{B} - <\underline{B}>_7|$, where $<>_7$ is a running 7 min average. As can be seen in the third panel of Figure 11 (note the logarithmic scale), the amplitude of the fluctuations is maximum in the CIR after the passage of the stream interface and it is reduced slightly in the high-speed wind that follows. This maximum of the fluctuations is in the compressed fast wind. The amplitude is minimum in the slow wind before the CIR and a transition is made across the CIR from low levels in the slow wind to high levels in the fast wind in a smooth manner. This distinct transition in the amplitude of turbulence across the CIR was also seen in the superposed averages of *Gosling et al.* [1978]. Other studies examining the turbulence across CIRs beyond 1 AU

**Figure 9.** Using OMNI2 measurements, superposed averages of the 14 CIRs in Table 1 that show evidence of rebound flows are plotted. In the first panel the transverse flow of the solar wind is plotted. Vertical dashed lines are added to demark the region of east-west flow deflection. In the second panel the perpendicular flow velocity in the local-Parker-spiral coordinate system is plotted. Vertical dashed lines are added to demark the region of rebound flow (away from the stream interface). In the third panel the ion entropy density of the plasma is plotted, and in the fourth panel the plasma vorticity is plotted. A vertical dashed line is added to indicate the time of peak vorticity.

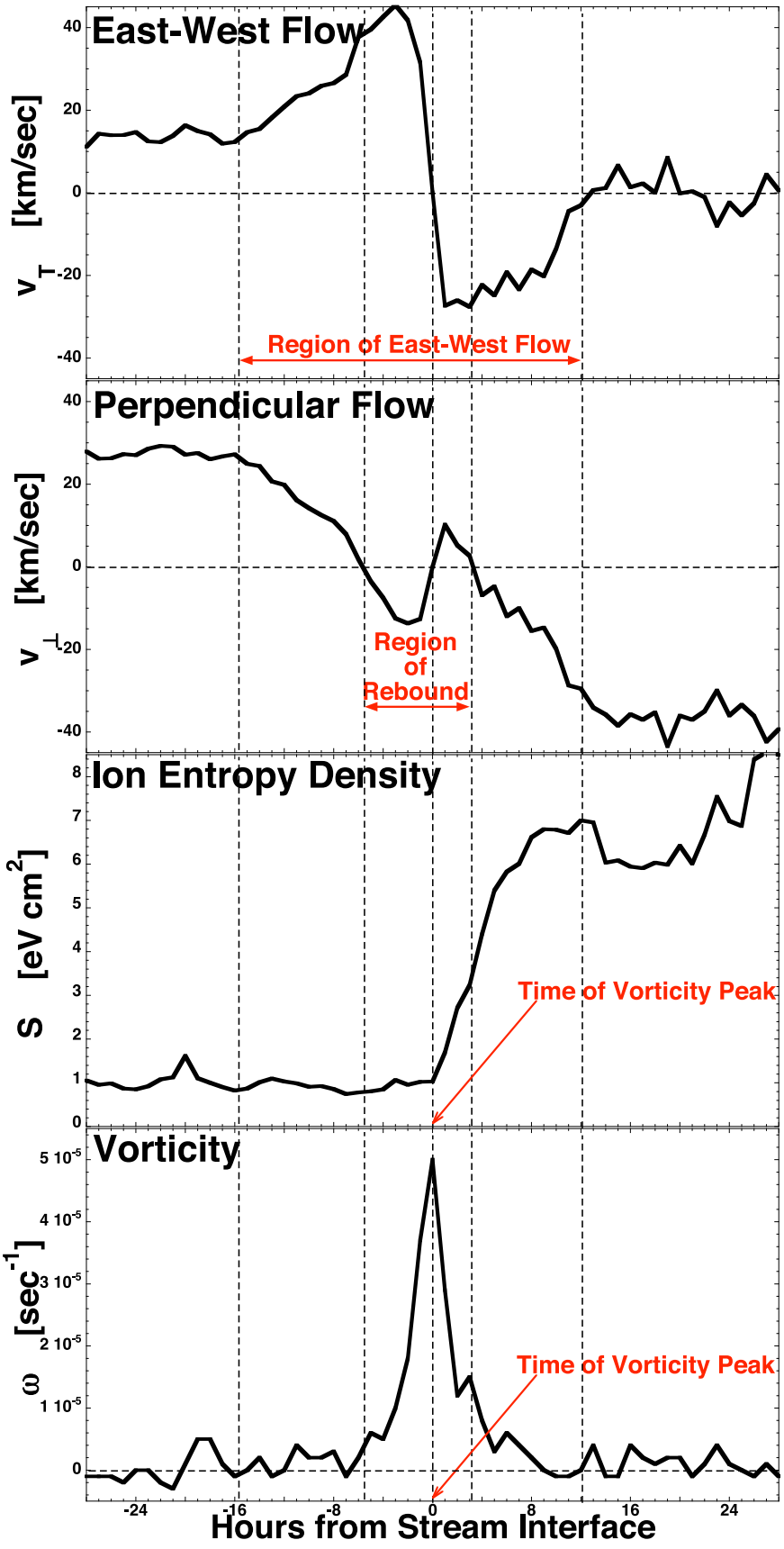
East-West Flow
$v_T$ [km/sec]
Region of East-West Flow
Perpendicular Flow
$v_\perp$ [km/sec]
Region of Rebound
Ion Entropy Density
S [eV cm$^2$]
Time of Vorticity Peak
Vorticity
$\omega$ [sec$^{-1}$]
Time of Vorticity Peak
Hours from Stream Interface

**Figure 9**

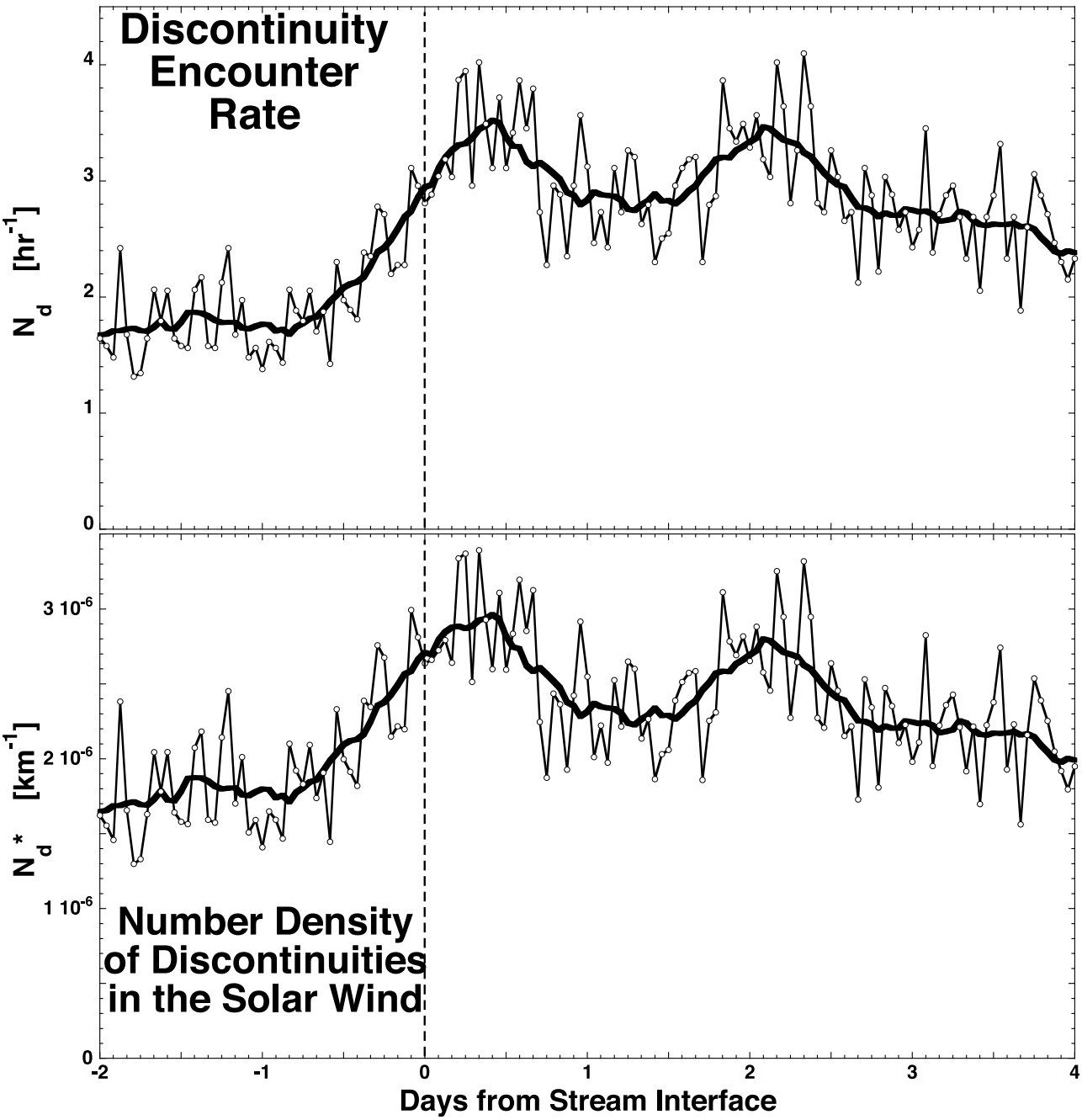


**Figure 10.** (top) Using ACE measurements for the 27 CIR events of Table 1, the superposed average of the number of strong discontinuities passing the spacecraft per hour is plotted. (bottom) The number density of strong discontinuities (number per distance perpendicular to the magnetic field) is plotted.

did [e.g., *Intriligator et al.*, 2001] or did not [e.g., *Horbury and Schmidt*, 1999; *Gulamali and Cargill*, 2001] see clear transitions from low levels in slow wind to high levels in fast wind across the CIRs; they did all see enhanced levels of turbulence within the > 1 AU CIRs owing to turbulence amplification/generation by the forward and reverse shocks.

[24] In the fourth panel of Figure 11 the normalized amplitudes $\delta B/B$ and $\delta v/v_A$ of the turbulence are plotted. The normalized amplitude is highest in the fast wind after the CIR passage, rather than in the compressed fast wind within the CIR. The normalized amplitudes make smooth transitions from low levels in the slow wind, increasing through the CIR, to high levels in the fast wind. When strong discontinuities are excluded from the amplitude measurements the difference in normalized amplitudes between the fast and the slow wind is only about a factor of 1.4.

[25] Note in the third and fourth panels of Figure 11 that the "turbulence amplitude" is higher if discontinuities are included (dashed curves) than if discontinuities are avoided. This is particularly true in the fast wind after the CIR passage (where the presence of Alfvenic discontinuities is well

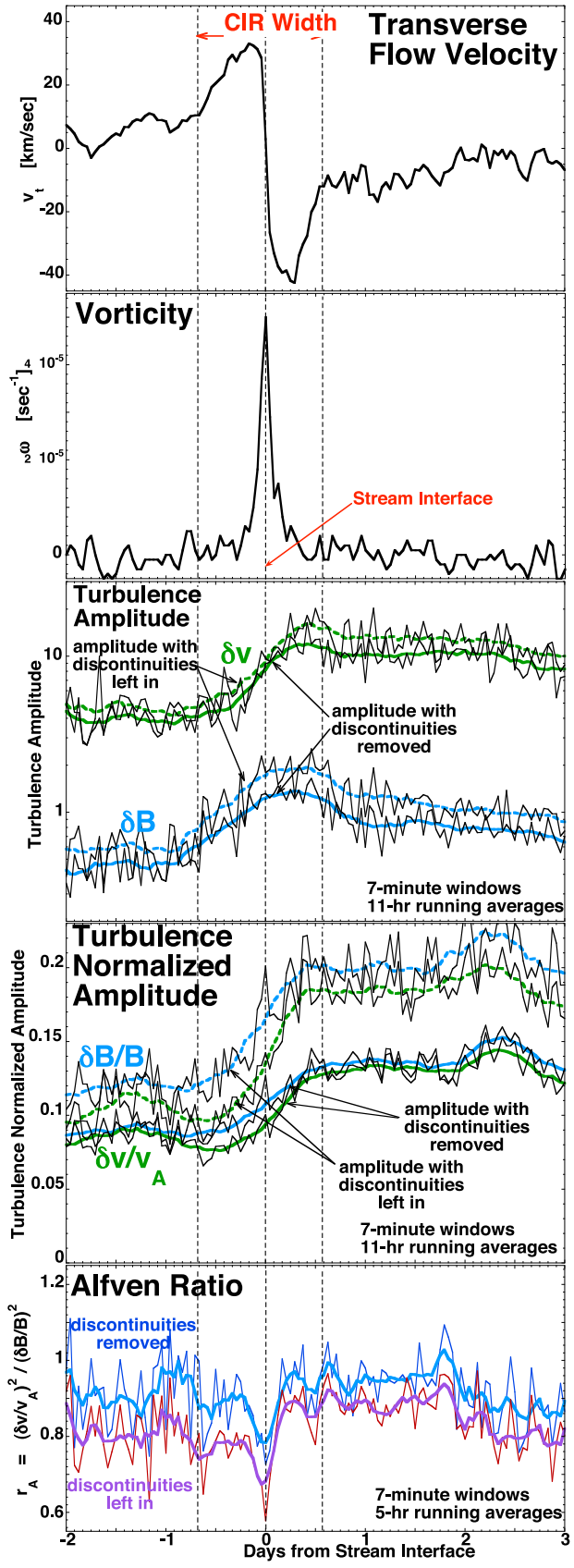


documented [e.g., *Tsurutani et al.*, 1994; *Tsurutani and Ho*, 1999; *Crooker and Gosling*, 1999]).

[26] In the fifth panel of Figure 11 the superposed average of the Alfven ratio $r_A$ in the 7 min band of frequencies is plotted, where $r_A = (\delta v/v_A)^2/(\delta B/B)^2$ is the ratio of the energy in velocity fluctuations to the energy in magnetic field fluctuations. The blue curve is the Alfven ratio excluding discontinuities and the violet curve is the Alfven ratio including discontinuities: the two thin curves have 1 h time resolution and the two thick curves are 5 h running averages. The Alfven ratio tends to be less than unity, with magnetic field fluctuations containing more energy than velocity fluctuations. As can be seen in the fifth panel of Figure 11, the Alfven ratio of the solar wind fluctuations is higher (closer to unity) if strong discontinuities are excluded from the data analysis. Also, the Alfven ratio $r_A$ has similar values in the slow and fast winds. A significant localized decrease in the Alfven ratio occurs coincident with the stream interface: at the steam interface in the 7 min band of frequencies the magnetic field fluctuations carry considerably more energy than do velocity fluctuations. At this time we do not have an explanation for this reduction.

### 4.3. Alfvenicity and Degree of $\underline{v}$-$\underline{B}$ Correlation

[27] The Alfvenicity is a measure of the degree and sign of correlation between the magnetic field fluctuations and the velocity fluctuations; the average of the Alfvenicity is a combined measure of (1) the degree of correlation between the velocity and field fluctuations and (2) the unidirectionality of fluctuation propagation along the magnetic field. To calculate the Alfvenicity of the solar wind the vector changes $\delta\underline{v}$ and $\delta\underline{B}$ of the velocity and magnetic field are measured with ACE at 64 s time resolution by taking 128 s differences in $\underline{v}(t)$ and $\underline{B}(t)$ according to $\delta\underline{v}(t) = \underline{v}(t+64) - \underline{v}(t-64)$ and $\delta\underline{B}(t) = \underline{B}(t+64) - \underline{B}(t-64)$. Similar to equation (1) of *Roberts et al.* [1987b], the signed Alfvenicity $\mathcal{A}(t)$ is calculated as

$$\mathcal{A} = s\,\delta\underline{v} \bullet \delta\underline{B}/|\delta\underline{v}||\delta\underline{B}|, \qquad (1)$$

where the sign $s(t) = +1$ if the IMF is away from the Sun and $s(t) = -1$ if the IMF is toward the Sun. The toward/away

**Figure 11.** Using ACE measurements, superposed averages of the amplitude and Alfven ratio of solar wind fluctuations are plotted for the 27 CIRs of Table 1. The zero epoch is the stream interface (vertical dashed line), and vertical dashed lines are added to demark the width of the CIR as determined by the east-west flow deflection. In the first panel the transverse velocity of the solar wind is plotted, and in the second panel the plasma vorticity is plotted. In the third and fourth panels the unnormalized amplitudes (third panel) and normalized amplitudes (fourth panel) of the magnetic field (blue) and velocity (green) fluctuations are plotted: the thin curves are 1 h time resolution, the thick dashed curves are 11 h running averages for all measurements, and the thick solid curves are 11 h running averages for measurements with strong discontinuities removed. In the fifth panel the Alfven ratio is plotted, with the thin curves being 1 h resolution and the thick curves being 5 h running averages: the red curves are for all measurements, and the blue curves are for measurements with strong discontinuities removed.

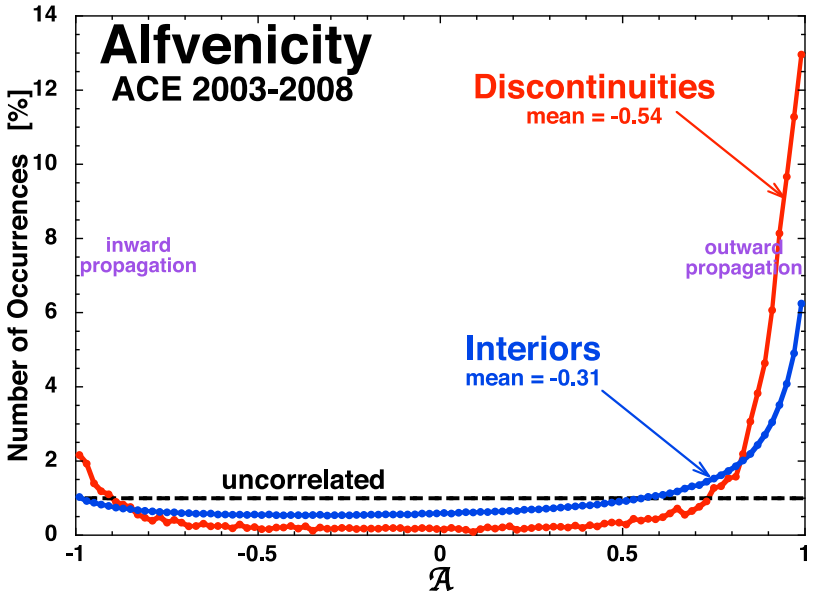


**Figure 12.** For 5.5 years of ACE measurements, the signed Alfvenicity is binned for 128 s differences $\delta\underline{v}$ and $\delta\underline{B}$. The red curve is for the strong discontinuities in the data set, and the blue curve is for the solar wind plasma between the discontinuities. The signed Alfvenicity is the cosine of the angle between the $\delta\underline{B}$ vector and the $\delta\underline{v}$ vector, with the +1 direction representing outward sense of propagation and the −1 direction representing the inward sense. The horizontal black dashed line is the expected distribution of signed Alfvenicity if $\delta\underline{v}$ and $\delta\underline{B}$ are completely uncorrelated (random directions).

nature of the IMF is calculated by examining the direction of $\underline{B}(t)$ relative to the predicted Parker-spiral direction. Defined according to equation (1), $\mathcal{A} = +1$ for an outward propagating Alfven wave and $\mathcal{A} = -1$ for an inward propagating Alfven wave.

[28] In Figure 12 the Alfvenicity $\mathcal{A}(t)$ is binned for 5.5 years of ACE measurements. The blue curve is the distribution of $\mathcal{A}$ for all times excluding times when discontinuities are passing over ACE (the "interiors" of flux tubes in a flux tube picture [*Borovsky*, 2008]) and the red curve is the distribution of $\mathcal{A}$ only for times when discontinuities (as defined in section 2) are passing ACE. Note that when discontinuities are removed, only the very strong discontinuities (with rotation angles greater than 45°) are removed: medium-sized discontinuities remain in the distribution. The horizontal dashed line in Figure 12 is the expected distribution of $\mathcal{A}$ for completely uncorrelated $\delta\underline{v}$ and $\delta\underline{B}$. As can be seen by comparing the red and blue curves, the distribution of Alfvenicity values differs for the solar wind discontinuities and the plasma between the discontinuities. Both distributions show correlation (a concentration of values near +1 or −1) and both tend toward the outward-propagation sense of correlation, but the solar wind discontinuities show a higher degree of $\delta\underline{v}$ $\delta\underline{B}$ correlation than the fluctuations between the discontinuities and the solar wind discontinuities show a stronger dominance of outward propagation than do the fluctuations between the discontinuities.

[29] In Figure 13 (top) the superposed average of the signed Alfvenicity $\mathcal{A}$ (defined in equation (1)) measured by ACE is plotted for the 27 CIR events of Table 1, with the zero epoch being the passage of the stream interface. The black curves are for all measurements and the red curves are for measurements during times when discontinuities are passing; the thin curves are 1 h averages of the superposed measurements and the thick curves are 7 h running averages of the thin curves. As can be seen in the black curve in Figure 13 (top), in the slow wind before the passage of the CIR the Alfvenicity $\mathcal{A}$ of the solar wind plasma is low (weakly correlated) and positive (outward sense), the Alfvenicity rises slightly in the compressed-slow-wind portion of the CIR, the Alfvenicity rises strongly across the compressed-fast-wind portion of the CIR, and the Alfvenicity of the solar wind plasma is high (stronger correlation) and positive (outward sense) in the fast wind after the passage of the CIR. These trends reflect the findings of *Belcher and Davis* [1971] and *Belcher and Solodyna* [1975] that the slow wind is not as Alfvenic as the fast wind and support the findings of *Tsurutani et al.* [1995], who observed lower Alfvenicity inside (shocked) CIRs beyond 1 AU than in the fast wind following those CIRs. The red curve (discontinuities only) in Figure 13 (top) reflects the same trends, but with higher correlations and a stronger outward dominance.

[30] To focus on the degree of correlation between $\delta\underline{v}$ and $\delta\underline{B}$, the superposed-epoch average of the absolute value $|\mathcal{A}|$ of the Alfvenicity is examined in Figure 13 (bottom). The absolute value $|\mathcal{A}|$ does not reflect the degree of inward or outward propagation, rather it measures the degree of correlation between $\delta\underline{v}$ and $\delta\underline{B}$. Averages of completely uncorrelated $\delta\underline{v}$ and $\delta\underline{B}$ result in $|\mathcal{A}| = 0.5$ and averages of fully correlated or fully anticorrelated $\delta\underline{v}$ and $\delta\underline{B}$ result in $|\mathcal{A}| = 1.0$. As a measure of the degree of correlation the quantity $2(|\mathcal{A}|-0.5)$ is used, which varies from 0 for uncorrelated $\delta\underline{v}$ and $\delta\underline{B}$ to 1 for completely correlated $\delta\underline{v}$ and $\delta\underline{B}$. In Figure 13 (bottom) the superposed average of $2(|\mathcal{A}|-0.5)$ is plotted.

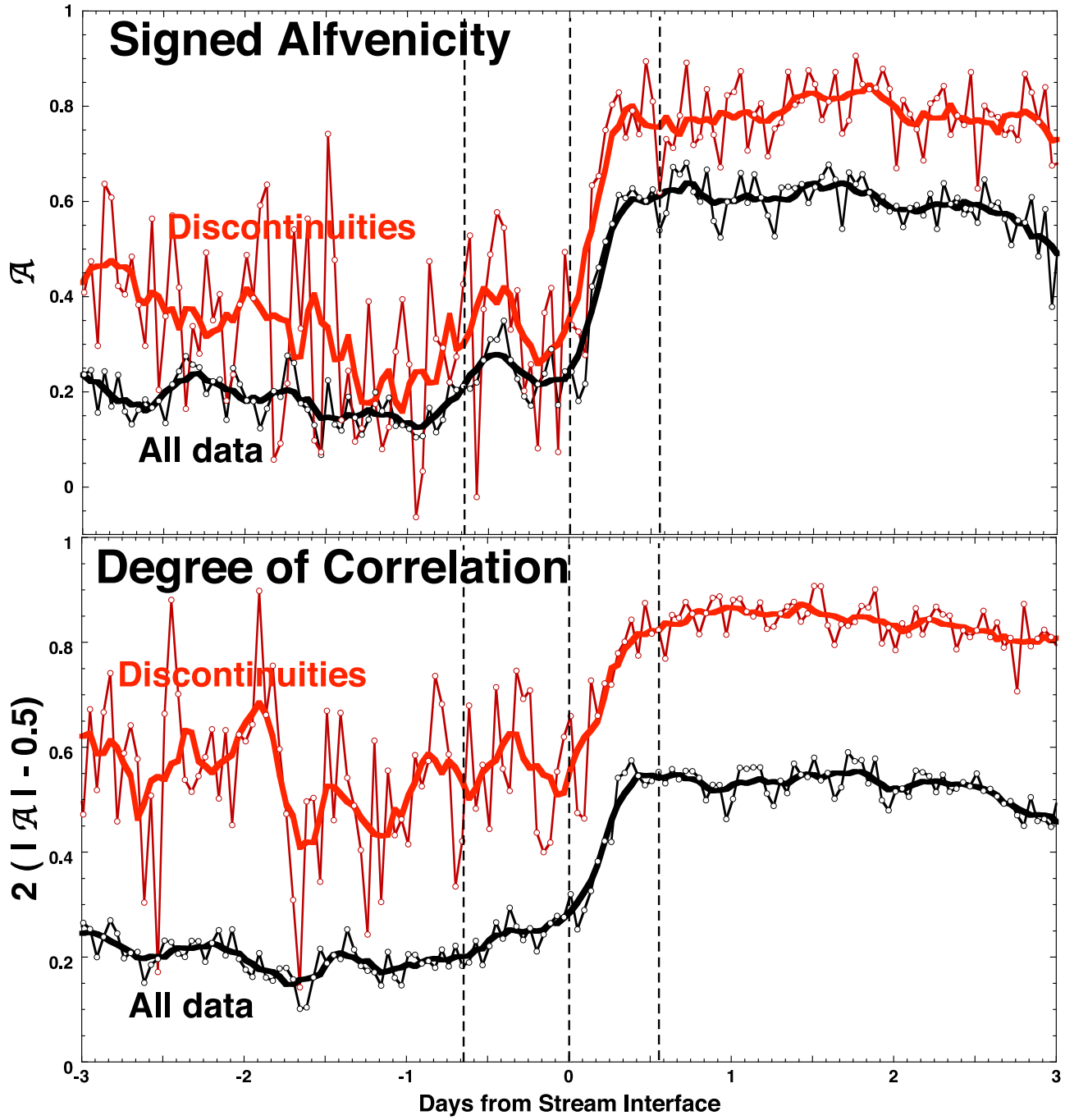


**Figure 13.** Using ACE measurements, the superposed average of the Alfvenicity of the solar wind is plotted across the 27 CIRs of Table 1 using 128 s differences $\delta\underline{v}$ and $\delta\underline{B}$. (top) The signed Alfvenicity is plotted. (bottom) The absolute value of the signed Alfvenicity is plotted. The zero epoch (vertical dashed line) is the passage of the stream interface. The black curves are all data, and the red curves are strong discontinuities: the thin curves have 1 h resolution, and the thick curves are 13 h running averages of the thin curves.

The black curves are for all measurements and the red curves are for measurements during times when discontinuities are passing. As can be seen by comparing the red and black curves in Figure 13 (bottom), the degree of correlation is higher for the discontinuities; this larger correlation coefficient could be owed in part to the fact that larger signals are more difficult to decorrelate with noise. The solar wind before the CIR show relatively poor $\delta\underline{v}$ $\delta\underline{B}$ correlation. In Figure 13 (bottom) the solar wind plasma and the discontinuities in the plasma show higher degrees of $\delta\underline{v}$ $\delta\underline{B}$ correlations in the fast wind after the CIR passes than in the slow wind before the CIR passes, with the degree of correlation increasing smoothly across of the CIR.

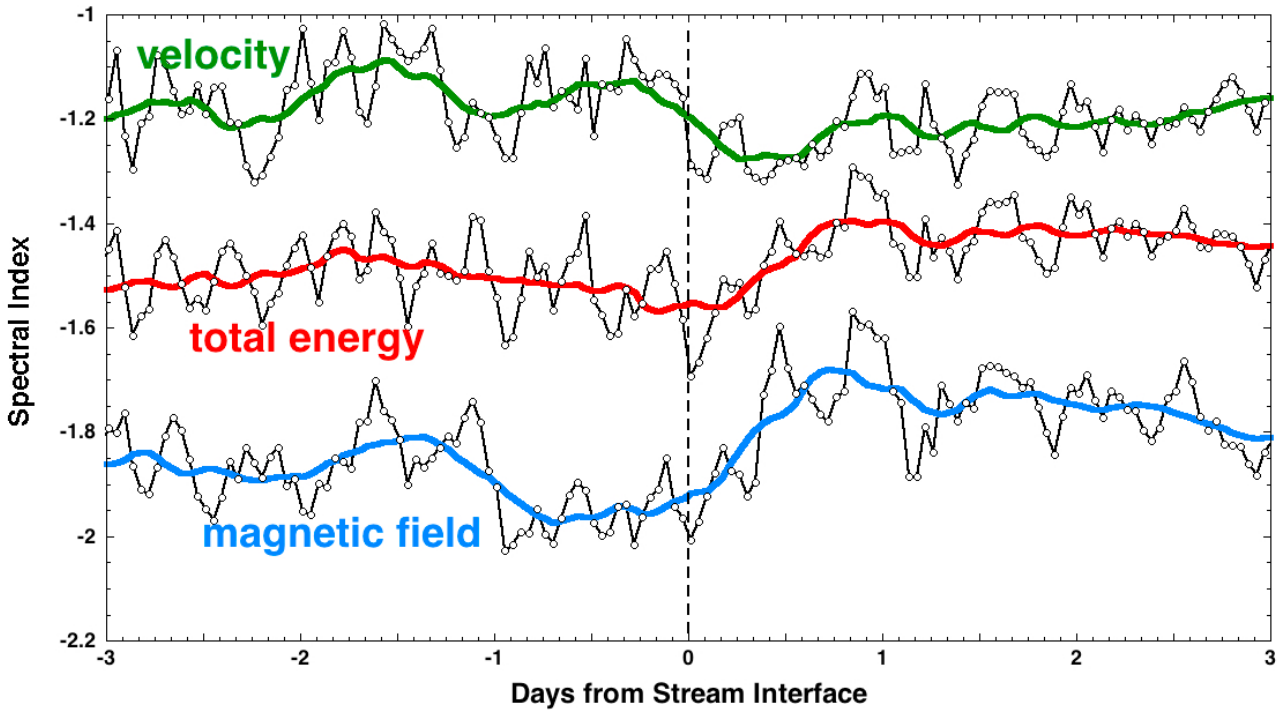


**Figure 14.** Using ACE velocity and magnetic field measurements with 64 s time resolution, the spectral slopes in the frequency range $4.3 \times 10^{-4} - 1.9 \times 10^{-3}$ Hz are fit to 4.55 h data intervals, and the resulting slopes are superposed-epoch analyzed for the 27 CIRs of Table 1. The zero epoch (vertical dashed line) is the passage of the stream interface, and the width of the CIR as determined by the transverse solar wind deflection is denoted by the outer vertical dashed lines. The superposed average of the magnetic field spectral slope is plotted in blue, the superposed average of the velocity spectral slope is plotted in green, and the superposed average of the total-energy spectral slope is plotted in red: thin curves have 1 h resolution, and thick curves are 13 h running averages of the thin curves.

### 4.4. Turbulence Spectral Indices

[31] In Figure 14 the superposed averages of the spectral slopes of the solar wind fluctuations are plotted. Fourier analysis of the ACE measurements is performed as follows. The entire 1998–2008 ACE data set is broken into 20,070 nonoverlapping 4.55 h long subintervals and each subinterval is analyzed separately. A 4.55 h interval consists of 256 measurements separated by 64 s, which is the time resolution of the SWEPAM plasma instrument on ACE. Since 256 is a power of 2, using data records that are 256 points long makes for efficient and accurate (no leakage) Fourier transforms. The subinterval length of 4.55 h is comparable to the correlation time of the solar wind turbulence in the reference frame of the satellite, which is 0.7–4 h [*Jokipii and Coleman*, 1968; *Matthaeus and Goldstein*, 1982a; *Tu and Marsch*, 1995b; *Matthaeus et al.*, 1999, 2005; *Feynman et al.*, 1996; *Richardson and Paularena*, 2001] for the magnetic field fluctuations, and perhaps twice as long for the velocity fluctuations [*Matthaeus and Goldstein*, 1982a]. The selection of 4.55 h ensures that the data subinterval is long enough to cover the inertial range of the solar wind turbulence. The 4.55 h is somewhat shorter than the 5–40 h autocorrelation times for the properties of the solar wind plasma (compare Figure 6 of *Borovsky et al.* [1998] and Figure 12 of *Borovsky and Funsten* [2003b]) so that the individual Fourier transforms tend not to contain mixtures of turbulence from different plasmas. Caution must be exercised, however, since 4.55 h long intervals admit several solar wind discontinuities into the interval, which can alter the analysis of turbulence [cf. *Borovsky*, 2008]. Data dropouts in the ACE magnetic field and plasma measurements are replaced by linear interpolation across the data gap. A record is kept of which subintervals have magnetic field-data replacements and which subintervals have plasma-data replacements. If 20 or more data points in a 256-point subinterval need to be replaced by interpolation, that subinterval is eliminated from the analysis. Each data subinterval is detrended prior to Fourier analysis. The detrending of the time-dependent data f(t) is done by subtracting a line g(t) from f(t) where the line goes through the endpoints $f(t_{min})$ and $f(t_{max})$ of the subinterval; the line is $g(t) = f(t_{min}) + (t-t_{min})(f(t_{max})-f(t_{min}))$. The purpose of the detrending is to eliminate the jump in the data when the ends of the subinterval are joined by the assumption of periodicity in the Fourier analysis. No test of the stationarity of the turbulence is made [e.g., *Matthaeus and Goldstein*, 1982b; *Matthaeus et al.*, 1986]. Rather, directional discontinuities are counted and a record is kept of the number of discontinuities in each subinterval. Each data subinterval is analyzed separately and the resulting parameters from the ensemble of subintervals are then averaged for the superposed epoch.

[32] To obtain power spectral densities (PSDs) of the detrended turbulent fluctuations, standard fast-Fourier-transform (FFT) methods are used [*Cooley and Tukey*, 1965; *Otnes and Enochson*, 1972]. No windowing or band-pass filtering is used prior to analysis, rather the data in each subinterval is detrended by subtracting a line. The power-spectral density PSD is obtained directly from the fast Fourier transform FFT via $PSD(v) = 2\Delta t/N\{[FFT(v_r)]^2 + [FFT(v_t)]^2 + [FFF(v_n)]^2\}$ and $PSD(B) = 2\Delta t/N\{[FFT(B_r)]^2 + [FFT(B_t)]^2 + [FFT(B_n)]^2\}$ where $\Delta t = 64$ s is the data time resolution and N = 256 is the number of data points in a Fourier transform (compare section 2.6 of *Borovsky et al.* [1997] or equation (5.6) of *Otnes and Enochson* [1972]). For the velocity power spectral density and the magnetic field power spectral density, least squares linear fits in $\log_{10}(P)$ versus $\log_{10}(f)$ are made (where P is power spectral density and f is frequency) and the spectral slopes $d\log_{10}(P)/d\log_{10}(f)$ of the fits are recorded. The fits are made over the frequency range $4.3 \times 10^{-4} - 1.9 \times 10^{-3}$ Hz. This range is approximately in the middle of the inertial subrange of the solar wind turbulence. The lower limit $4.9 \times 10^{-4}$ Hz of this frequency range is chosen to stay a factor of about 2 away from the reported correlation times of the solar wind turbulence, which are 0.7–4 h [*Matthaeus and Goldstein*, 1982a; *Tu and Marsch*, 1995b; *Matthaeus et al.*, 1999; *Feynman et al.*, 1996]. The upper limit $1.9 \times 10^{-3}$ Hz of this frequency range is chosen to stay a factor of 4 away from the Nyquist frequency of the data, which for 64 s data resolution is $7.8 \times 10^{-3}$ Hz. The results of the T methods have been checked by repeating the analysis with the Blackman-Tukey method of computing PSDs [*Otnes and Enochson*, 1972]. The Blackman-Tukey method is much slower computationally than is the direct T method and the Blackman-Tukey method introduces leakage and negative power into the PSDs, which direct T methods do not. When the Blackman-Tukey method was used, leakage in the PSDs is reduced by first "prewhitening" the data and afterward "postdarkening" the PSD following the prescription of *Bieber et al.* [1993]. The direct T method and the Blackman-Tukey method give statistically the same results for an ensemble of ACE data subintervals, although the individual PSDs from the two methods may differ.

[33] The fitted spectral slopes vary considerably from one data interval to the next, making interpretation unreliable if only a few spectra are used across a CIR. Superposed averaging reduces the variability and brings out the systematic trends in the spectra across CIRs.

[34] The three black curves in Figure 14 are the superposed averages of the spectral slopes of the power spectral densities of the velocity fluctuations $\delta$v, the magnetic field fluctuations $\delta$B, and the total-energy fluctuations $\delta E = m_i n \delta v^2/2 + \delta B^2/8\pi$. The superposed averaging in Figure 14 utilizes ~850 Fourier-transformed time intervals (out of 20,070 intervals for the entire ACE merged plasma and field data set). The green, blue, and red curves in Figure 14 are 13 h running averages of the spectral slopes of the velocity, magnetic field, and total energy, respectively. Note that the mean value of the total-energy spectral index is near 3/2, consistent with a Kraichnan spectrum rather than a Kolmogorov spectrum [see also *Grappin et al.*, 1990; *Podesta et al.*, 2006]. (See also work by *Roberts* [2007] and D. A. Roberts (The evolution of the spectrum of solar wind magnetic and velocity fluctuations from 0.3 to 5 AU, submitted to *Journal of Geophysical Research*, 2010), who find that the <3/2 velocity spectra at 1 AU evolve into 5/3 spectra beyond 4 AU.)

[35] As can be seen in Figure 14 there is a systematic difference between the spectral slopes of the velocity fluctuations and the magnetic field fluctuations in the solar wind: the magnetic field spectral index tends to be steeper than the velocity spectral index. In fact, in the 20,070 intervals of ACE data analyzed, only 14% have a velocity spectral index that is steeper than the magnetic field spectral index. For the 20,070 4.55 h ACE intervals, the velocity and magnetic field spectral indices are cross-correlated with a linear correlation coefficient of $R_{corr} = +0.40$: that is, if a 4.5 h interval has a steeper than average magnetic field slope, that interval will tend to also have a steeper than average velocity slope. For MHD turbulence it has typically been assumed that the velocity fluctuations and the magnetic field fluctuations have statistically similar behaviors [cf. *Kraichnan*, 1965]; Figures 12 and 13 imply that this is more true of the solar wind discontinuities than it is for the solar wind turbulence between the discontinuities. An assessment of the reasons for the differences between the spectral slopes of velocity fluctuations and the spectral slopes of magnetic field fluctuations [cf. *Podesta et al.*, 2006] is left for a future report. Among the possible reasons considered are (1) nonlocal energy transfer in wave number space which may act on the $\delta$v spectrum but not on the $\delta$B spectrum [e.g., *Pouquet et al.*, 1976; *Debliquy et al.*, 2005; *Alexakis et al.*, 2005; *Mininni et al.*, 2005b], (2) compressibility changing the modal structure of the turbulence fluctuations [*Malara et al.*, 1997; *Carbone et al.*, 1992], (3) magnetization effects on spectral transfer [*Cattaneo*, 1994] and anisotropy [*Montgomery and Turner*, 1981; *Shebalin et al.*, 1983; *Goldreich and Sridhar*, 1997; *Oughton et al.*, 1998; *Cho and Vishniac*, 2000; *Milano et al.*, 2001], (4) plasma beta changing the modal structure of the turbulent fluctuations [*Gary*, 1993; *Cho and Lazarian*, 2005] and plasma beta changing the anisotropy of MHD turbulence [*Zank and Matthaeus*, 1993; *Matthaeus et al.*, 1996; *Ghosh and Goldstein*, 1997], (5) intermittency modifying the spectrum and spectral transfer of turbulence [*Carbone*, 1993; *Gomez et al.*, 1999; *Müller and Biskamp*, 2000], (6) the weakening of the Alfven effect at low-k weakening the coupling between the field and the flow [*Müller and Grappin*, 2004, 2005], and (7) weakening of nonlinear interactions at high-k caused by increased $\underline{v}$-$\underline{B}$ alignment [*Boldyrev*, 2006; *Podesta*, 2010; J. J. Podesta and A. Bhattacharjee, Theory of incompressible MHD turbulence with scale-dependent alignment and cross-helicity, submitted to *Physics of Plasmas*, 2010].

[36] In Figure 14, a few trends can be seen in the spectral slopes of the turbulence. The first is that the difference in slopes between $\delta$v and $\delta$B is less in the fast wind after the CIR passage than it is in the slow wind before the CIR passage. (This fast-wind/slow-wind difference was also noted by *Podesta et al.* [2006]). The reason for this trend is not known. Perhaps the change is a feature of nonturbulent outward propagating Alfven waves in the fast wind [e.g., *Dobrowolny et al.*, 1980; *Burlaga et al.*, 1982] versus well-developed MHD turbulence in the slow wind [*Klein et al.*, 1993; *Bruno*, 1997]. Or perhaps it is a feature of the greater dominance of Alfvenic discontinuities in the fast

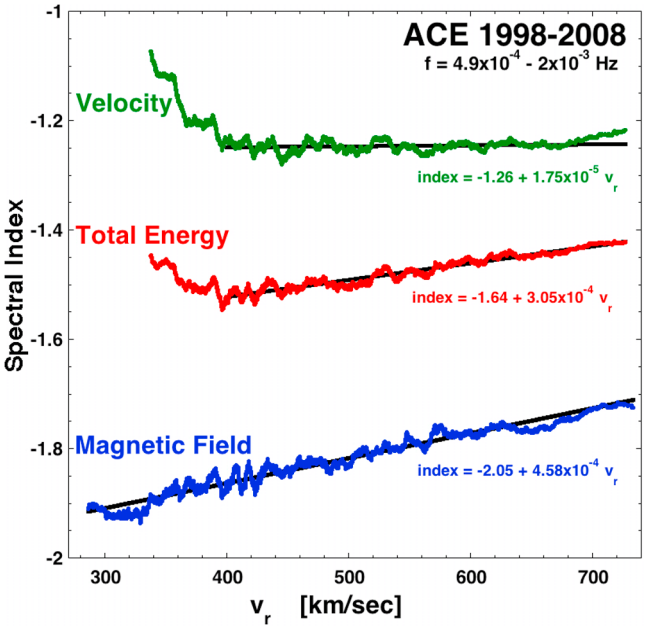


**Figure 15.** Using ACE velocity and magnetic field measurements with 64 s time resolution, the spectral slopes in the frequency range $4.3 \times 10^{-4} - 1.9 \times 10^{-3}$ Hz are calculated for 20,070 4.55 h data intervals. The spectral slopes are plotted as functions of the solar wind velocity, and 500-point running averages are calculated. The 500-point running averages appear in Figure 15: the velocity spectral slope is plotted in green, the magnetic field spectral slope is plotted in blue, and the total-energy spectral slope is plotted in red. Least squares linear regression fits to the data are indicated as the three black lines.

wind measurements than in the slow-wind measurements (see Figure 13). A second trend seen in Figure 14 is that the spectral index of the magnetic field (blue curve) tends to be slightly steeper in the slow wind prior to the CIR passage than in the fast wind after the CIR passage.

[37] To check these trends, the database of 20,070 Fourier-analyzed 4.5 h long intervals of ACE data from the years 1998–2008 is statistically analyzed. In Figure 15, 500-point running averages of the spectral slopes of the velocity (green), magnetic field (blue), and total energy (red) are plotted as functions of the average solar wind speed for each 4.5 h interval. A definite trend in the spectral index of the magnetic field versus the solar wind speed is seen in Figure 15, with faster wind having shallower spectral indices for the field fluctuations, as was seen in Figure 14. (This slow-wind/fast-wind trend was also found in the magnetic field spectral indices at 5 AU in Figure 3 of *Gulamali and Cargill* [2001].) In the 20,070-interval ACE database the magnetic field spectral index is positively correlated with the solar wind speed at the 8-$\sigma$ level of confidence. A linear-regression fit to the spectral index $S_B$ of the magnetic field versus solar wind speed $v_{sw}$ yields $S_B = -2.03 + 4.15 \times 10^{-4}\ v_{sw}$ where $v_{sw}$ is in km/s; this fit varies from −1.88 at 350 km/s to −1.72 at 750 km/s. In Figure 15, the spectral index of the velocity fluctuations is almost constant for solar wind velocities greater than 400 km/s and shows a flattening of the spectrum for velocities less than 400 km/s. An investigation of the ACE measurements for 25 of the flatter-spectra data intervals at low solar wind velocity finds that 72% are associated with depressed proton temperatures or counterstreaming strahl electrons. A depressed proton temperature here means that the measured temperature is lower than the temperature-velocity expressions $T = -0.134v_{sw}^2 + 490v_{sw} - 111000$ for $v_{sw}^2 < 450$ km/s and $T = -0.430v_{sw}^2 + 1003v_{sw} - 273000$ for $v_{sw} > 450$ km/s (R. Skoug, private communication, 2009) [see also *Lopez*, 1987; *Richardson and Cane*, 1995; *Elliott et al.*, 2005; *Borovsky and Steinberg*, 2006b], where T is in K and $v_{sw}$ is in km/s. Depressed temperatures are one indication of ejecta [*Gosling et al.*, 1973; *Richardson and Cane*, 1995; *Elliott et al.*, 2005] and counterstreaming strahl electrons can be evidence of closed-loop structures [*Bame et al.*, 1981; *Gosling et al.*, 1987; *Skoug et al.*, 2000], that is, ejecta. The conclusion of the inspection of the data intervals is that the shallow velocity spectral indices in Figure 15 are due in part to slow ejecta in the slow solar wind. Given the fact that the SWEPAM instrument on ACE can lack ion counts when the solar wind velocity goes very low (R. Skoug, private communication, 2009), measurement error at low solar wind speed could also contribute to produce the shallow spectral indices of the velocity fluctuations in Figure 15. Fitting the measured spectral indices $S_v$ of the velocity fluctuations for $v > 400$ km/s yields $S_v = -1.26 + 1.75 \times 10^{-5}$ v where v is in km/s; this fit varies from −1.253 at 400 km/s to −1.247 at 750 km/s. As can be seen in Figure 15, the spectral index of the total energy lies between the spectral indices of the magnetic field and the velocity. Note that the upturn in the velocity spectra at low solar wind speed also appears as an upturn in the total-energy spectral index. A linear-regression fit to the measured spectral indices $S_E$ of the total-energy fluctuations for $v > 400$ km/s yields $S_E = -1.64 + 3.05 \times 10^{-4}$ v where v is in km/s; this fit varies from −1.52 at 400 km/s to −1.41 at 750 km/s. (This slow-wind/fast-wind trend in the spectral index of the total energy is opposite to the finding of *Grappin et al.* [1990] wherein an anticorrelation was found between solar wind temperature and the total-energy spectral index.)

### 4.5. Elsasser Inward and Outward Propagating Fluctuations

[38] In Figure 16 the spectral slope and amplitudes of the superposed-epoch average of the Elsasser variables $\underline{z}^{\pm} = \underline{v} \pm \underline{b}$ are plotted, where $\underline{b} = \underline{B}/(4\pi m_i n)^{1/2}$. In Figure 16 (top) the spectral slopes in the frequency range $4.3 \times 10^{-4} - 1.9 \times 10^{-3}$ Hz are plotted. The thin curves have a resolution of 1 h in the superposed averages, but 4.5 h long data intervals go into the averaging. The thick curves are 13 h running averages. The inward-versus-outward direction of the IMF is calculated and the two Elsasser variables are labeled according to whether they represent inward traveling (toward the Sun) or outward traveling (away from the Sun) Alfven waves, following the convention of *Tu and Marsch* [1995a]. As can be seen in Figure 16 (top), the spectral slopes of inward and outward Elsasser variables are similar in the slow wind and in the compressed-slow-wind portion of the CIR, but the two spectral slopes differ substantially in the fast wind with the outward spectra being much flatter.

[39] In Figure 16 (middle) the RMS amplitudes of the two Elsasser spectra in the frequency range $f \geq 1 \times 10^{-3}$ Hz are plotted. As can be seen, in the slow wind and in the com-

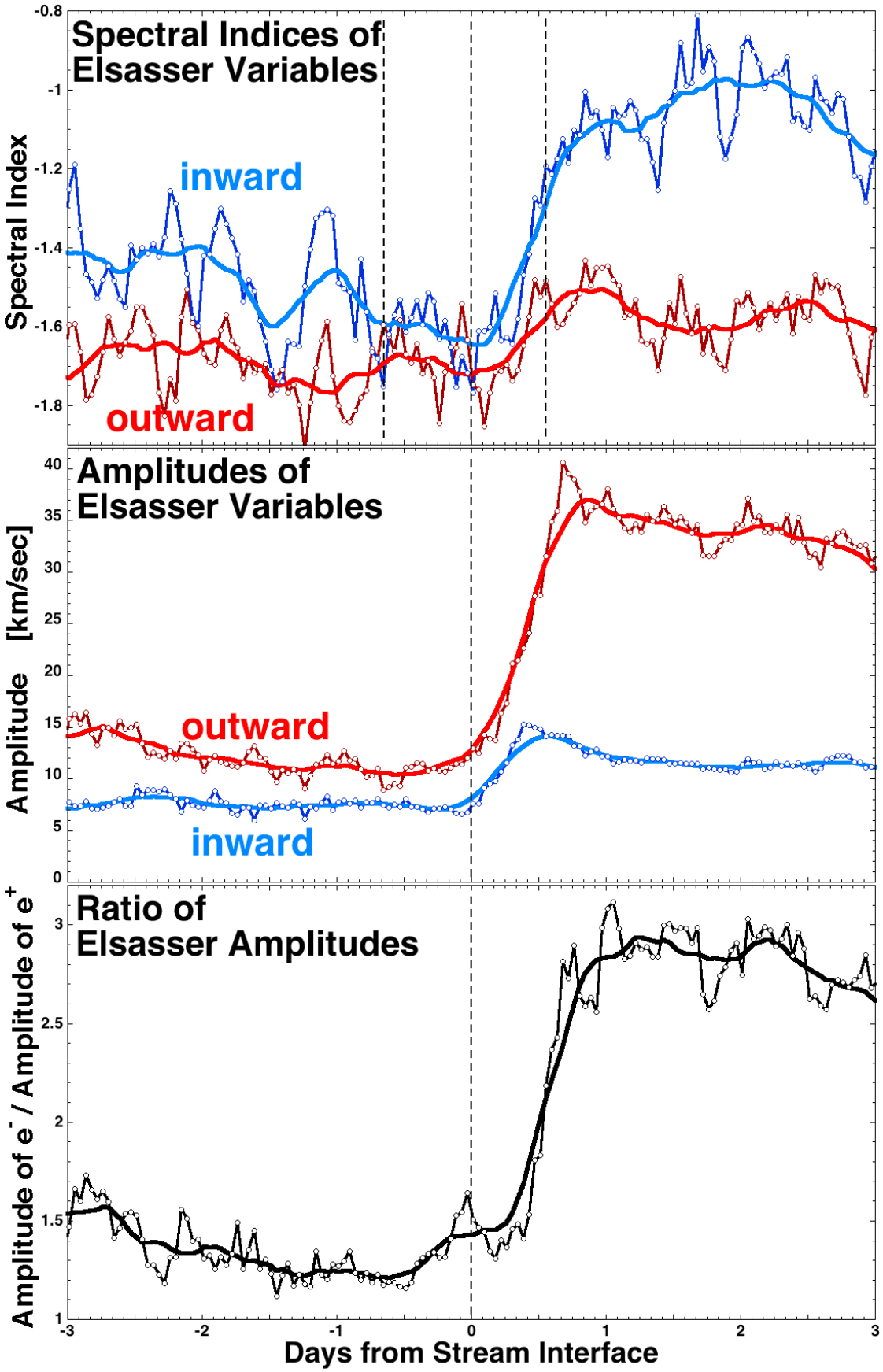
Spectral Indices of Elsasser Variables
Spectral Index
inward
outward
-0.8
-1
-1.2
-1.4
-1.6
-1.8
Amplitudes of Elsasser Variables
Amplitude [km/sec]
outward
inward
40
35
30
25
20
15
10
5
0
Ratio of Elsasser Amplitudes
Amplitude of e⁻ / Amplitude of e⁺
3
2.5
2
1.5
1
-3
-2
-1
0
1
2
3
Days from Stream Interface

**Figure 16**

pressed-slow-wind portion of the CIR the outward amplitude dominates slightly, in the fast wind the outward amplitude dominates greatly, and a smooth transition between the two states occurs across the compressed-fast-wind portion of the CIR. Note that the amplitude of the inward fluctuations less than doubles in going from the slow wind into the fast wind, whereas the amplitude of the outward fluctuations is about three times higher in the fast wind than it is in the slow wind. This large variation in the outward power compared with a smaller variation in the inward power was noted by *Tu et al.* [1990]. Looking at two CIRs (one at 0.3 AU and the other at 1.0 AU), *Tu et al.* [1990] reported an increase in the amplitude of inward propagating Elsasser fluctuations associated with CIR shear: no such increase is seen in Figure 16. Note in Figure 12 that the Alfvenicity of the discontinuities of the solar wind is higher than the Alfvenicity of the solar wind plasma in general, in the sense that the discontinuities show more dominance of outward propagation than the plasma in general does: for Figure 16 this implies that some of the dominance of the outward-Elsasser amplitude could be owed to discontinuities in the solar wind rather than Alfven waves or turbulence [see also *Neugebauer et al.*, 1984, 1986; *Neugebauer*, 1985].

[40] In Figure 16 (bottom) the ratio of the amplitudes of outward-to-inward Elsasser-variable fluctuations in the $f \geq 1 \times 10^{-3}$ Hz band of frequencies is plotted. In the slow wind the ratio is slightly above unity, meaning that outward traveling fluctuations slightly dominate over inward traveling (see also Figure 13, top). In the fast wind, outward traveling fluctuations strongly dominate (compare Figure 13). The strong dominance of "outward propagation" in the fast wind and a weaker domination in the slow wind is well known [e.g., *Belcher and Davis*, 1971; *Belcher and Solodyna*, 1975; *Horbury and Schmidt*, 1999; *Gulamali and Cargill*, 2001]. In the CIR itself, Figure 16 shows that the inward/outward dominance is similar to that in the slow wind, with outward traveling fluctuations slightly dominating as in the slow wind. The higher-resolution thin curve in Figure 16 (bottom) may indicate an enhancement in the dominance of outward propagation localized about the stream interface, although the deviation in the thin curve might not be statistically significant.

## 5. Driving of Turbulence in Shear

[41] In section 5.1, arguments are presented that imply that the spreading of turbulence away from the location where it is driven is quite limited. In section 5.2 the superposed-epoch averages are examined for signatures of driving.

### 5.1. Spreading of Turbulence During the Lifetime of the Solar Wind

[42] If the MHD turbulence of the solar wind is created in shear zones, then in the ~100 h lifetime of the solar wind plasma at 1 AU the spread of that turbulence away from the source of driving will be limited along the ambient magnetic field and the spread will be strongly limited across the field. Any shear-flow perturbation in the MHD frequency regime will propagate along the magnetic field ducted as an Alfven wave [*Alfven and Falthammar*, 1963; *Drell et al.*, 1965; *Fejer and Lee*, 1967; *Goertz and Boswell*, 1979]. Models of MHD turbulence often explicitly account for the propagating nature of the turbulent fluctuations [e.g., *Kraichnan*, 1965; *Matthaeus and Zhou*, 1989], even when the fluctuations have wave vectors nearly perpendicular to the magnetic field [e.g., *Goldreich and Sridhar*, 1997; *Boldyrev*, 2006]. For flow fluctuations with wave vectors nearly perpendicular to the magnetic field, the group velocities are still along the magnetic field as long as the perpendicular wavelengths are larger than the kinetic scales of gyroradii and skin depths [*Morales and Maggs*, 1997; *Vincena et al.*, 2004]. (That is, unless the perturbation couples to a compressive fluctuation, which can propagate across the magnetic field as a magnetosonic (fast) perturbation.) Any flow created in the plasma will spread along the magnetic field owing to this ducted propagation [*Borg et al.*, 1985; *Leneman et al.*, 1999; *VanZeeland et al.*, 2001]. However, for turbulence to spread across the magnetic field, eddy diffusion must act [e.g., *Ueno et al.*, 2001; *Frank et al.*, 2001; *Branover et al.*, 2004].

[43] In Figure 17, the limit on the spreading of the turbulence is quantified. For MHD turbulence comprised of Alfvenic fluctuations, the distance a perturbation can move along the magnetic field is limited by the Alfven speed $v_A$ of the plasma. In the age $\tau_{age}$ of the solar wind (where $\tau_{age}$ is the chronological age of the solar wind rather than the "dynamical age" [e.g., *Matthaeus et al.*, 1998]), the distance of propagation along the field is

$$L_{\|} = v_A \tau_{age}. \quad (2)$$

Taking $\tau_{age}$ = 1 AU/$v_{sw}$ with the superposed average of $v_{sw}$ given as a function of time in the first panel of Figure 4, and with the superposed average of $v_A$ given as a function of time in the fourth panel of Figure 4, $L_{\|}$ is calculated and plotted as a function of time in Figure 17 (top). As can be seen, the turbulence can spread along the ambient magnetic field to a distance of more than $10^7$ km away from the source of driving at 1 AU in the lifetime of the solar wind plasma. In a CIR the magnetic field lies in the plane of the

**Figure 16.** Using ACE velocity and magnetic field measurements with 64 s time resolution, the spectral slopes in the frequency range $4.3 \times 10^{-4} - 1.9 \times 10^{-3}$ Hz are fit to 4.55 h data intervals, and the resulting slopes are superposed-epoch analyzed for the 27 CIRs of Table 1. (top) The superposed average of the outward-Elsasser-variable spectral slope is plotted in red, and the superposed average of the inward-Elsasser-variable spectral slope is plotted in blue. (middle) The superposed averages of the amplitude of the outward (red) and inward (blue) Elsasser-variable fluctuations are plotted for the frequency range $f \geq 1 \times 10^{-3}$ Hz. (bottom) The superposed average of the ratio of the amplitude of the outward to inward Elsasser-variable amplitudes is plotted. In all cases the thin curves have 1 h resolution, and the thick curves are 13 h running averages of the thin curves. The zero epoch (vertical dashed line) is the passage of the stream interface; the width of the CIR as determined by the transverse solar wind deflection is denoted by the outer vertical dashed lines.

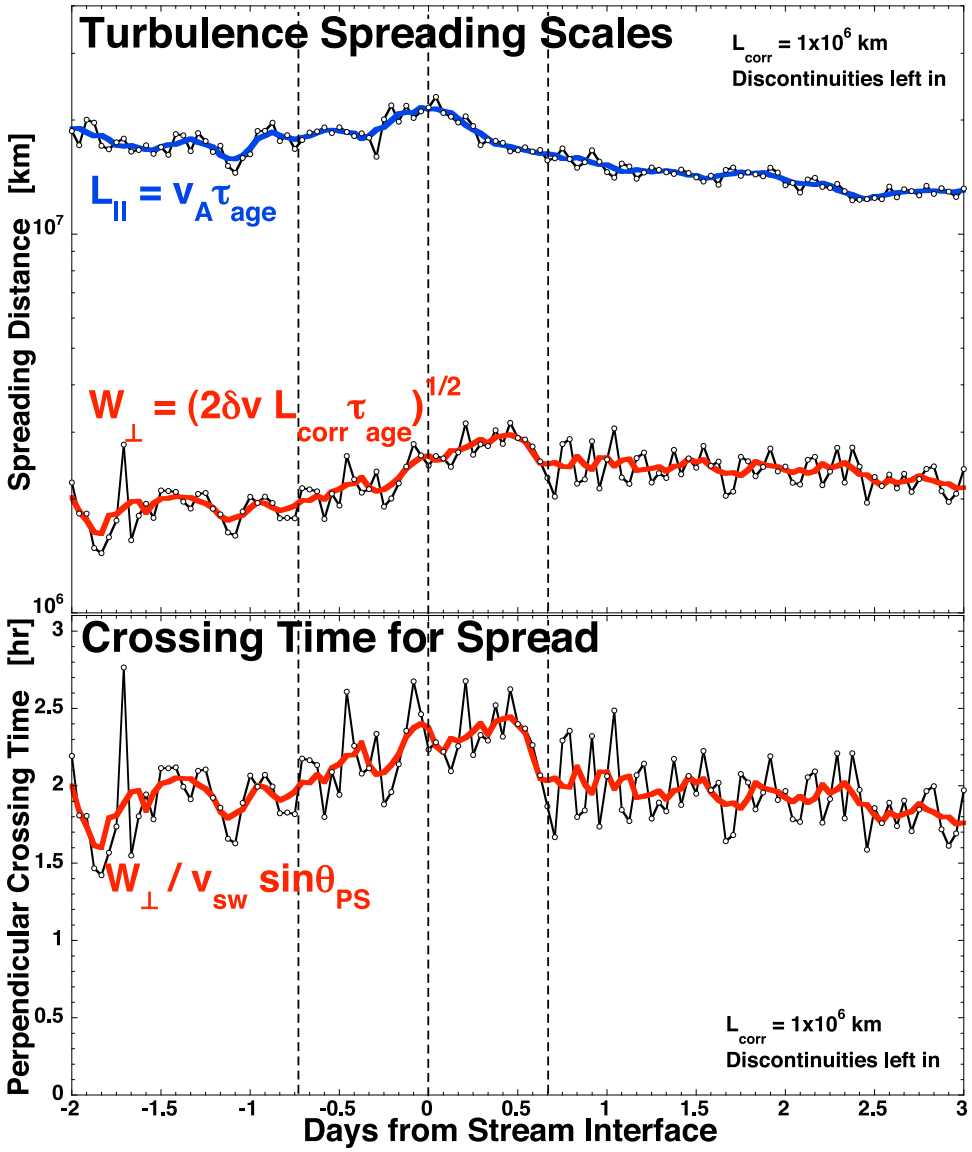


**Figure 17.** From parameters of the solar wind and its fluctuation amplitudes for the 27 CIRs of Table 1, the distance that turbulence can spread in the age of the solar wind plasma is calculated and plotted across the CIRs. (top) The spreading distance in kilometers along the magnetic field (blue) and across the magnetic field (red) are plotted. (bottom) The satellite crossing time at 1 AU for the perpendicular spreading distance is plotted. In the plots the thin curves have 1 h resolution, and the thick curves are 5 h running averages of the thin curves.

stream interface [e.g., *Clack et al.*, 2000]: this means that if the turbulence is driven at the stream interface, this parallel-to-B spreading will keep the turbulence at the stream interface.

[44] The spreading of turbulence transverse to the magnetic field of the solar wind will be much more restricted, diffusing across the field a distance that varies as the square root of the age of the wind. The MHD eddy-diffusion coefficient $D_{\perp\perp}$ [*Chen and Montgomery*, 1987; *Ishizawa and Hattori*, 1998; *Yoshizawa and Yokoi*, 1996; *Borovsky*, 2006] for turbulent transport across the field will be approximately $D_{\perp\perp} = (\delta x)^2/\delta t \approx (\delta v\ \tau_{corr})^{\ 2}/\tau_{corr} = (\delta v)^2\tau_{corr}$ where $\delta v$ is the amplitude of the turbulent fluctuations and $\tau_{corr}$ is the correlation time (large-eddy turnover time) in the reference frame of the plasma. (If there is suppression of the turbulent transport by the mean magnetic field or by the shear layer [cf. *Kim et al.*, 2001; *Douglas et al.*, 2008; *Newton and Kim*, 2009] then the eddy-diffusion coefficient will be less than $(\delta v)^2\tau_{corr}$.) A measure of the turbulence amplitude $\delta v$ is given in the second panel of Figure 11. The turbulence correlation time $\tau_{corr}$ in the reference frame of the plasma is difficult to obtain. It is approximately $L_{corr}/\delta v$, where $L_{corr}$ is the measured correlation length of the turbulence, giving $D_{\perp\perp} \approx (\delta v)^2\tau_{corr} \approx \delta v L_{corr}$. For our estimates of the turbulence spreading, we will take $L_{corr} = 1 \times 10^6$ km independent of the type of solar wind [*Jokipii and Coleman*, 1968; *Matthaeus and Goldstein*, 1982a; *Tu and Marsch*, 1995b; *Matthaeus et al.*, 1999; *Feynman et al.*, 1996; *Borovsky and*

*Gary*, 2009]. The diffusion equation that describes the spreading is $\partial f/\partial t = D_{\perp\perp}\,\partial^2 f/\partial x^2$: accordingly, in the age of the wind $\tau_{age}$ the turbulence will spread across the field a distance $W_\perp$ given by $1/\tau_{age} = D_{\perp\perp}/W_\perp^2$. Solving for $W_\perp$ yields the spreading distance $W_\perp = (D_{\perp\perp}\,\tau_{age})^{1/2}$. With $D_{\perp\perp} = (\delta v)^2\tau_{corr} = \delta v L_{corr}$, this is

$$W_\perp = \left(\delta v L_{corr}\tau_{age}\right)^{1/2}. \quad (3)$$

Using $\delta v$ from Figure 11, $\tau_{age}$ = 1 AU/$v_{sw}$ with $v_{sw}$ from Figure 4, and $L_{corr} \sim 1 \times 10^6$ km, the value of $W_\perp$ is plotted in Figure 17 (top) as a function of time through the CIR. As can be seen, values of $\sim 10^6$ km are obtained in the slow wind, the fast wind, and in the CIR.

[45] In the Figure 17 (bottom) the estimated thickness of the spreading transverse to the field is replotted in terms of the time $\tau_{cross}$ required for a spacecraft to cross the region of width $W_\perp$ traveling at $v_{sw}$, expressed as $\tau_{cross} = W_\perp/v_{sw}$ sin $\theta$ where $\theta$ = arctan(405/$v_{sw}$) is the Parker-spiral angle from radial. As can be seen in this plot, the spreading layer is only about 2 h wide as seen by a spacecraft. Hence, if turbulence is driven by a shear layer, in our superposed-epoch plots that driven turbulence will be very localized around the location of that shear layer.

### 5.2. Evidence for Turbulence Driven by Shear

[46] If shear is an important driver of the turbulence of the solar wind, then one should expect to see the level of turbulence enhanced at a strong, long-lived shear zone such as the stream interface, or to see the properties of the solar wind fluctuations change abruptly at the shear zone. In this section we will look for any signature that is different at the shear zone as compared with the neighboring plasmas (the fast and slow wind). If a difference is found, we will attempt to interpret the role of shear in that difference. Expected spatial scales of turbulence driven by stream-interface shear zones at 1 AU are discussed in Appendix A. For the data collected in this superposed-epoch study, evidence for the driving of solar wind turbulence by shear would be (1) an enhanced amplitude of turbulence at or very close to the shear zone, (2) an indication in the inward-outward Elsasser variables that the turbulence is more fully developed near the shear zone, (3) unusual signatures in the $\delta v$ and $\delta B$ spectra indicating a change in the driving near the shear zone, (4) a decrease in the Alfvenic correlations between velocity fluctuations and magnetic field fluctuations implying Alfven-wave conversion at the shear zone, or (5) a localized specific-entropy signature near the shear zone indicating ion heating by spectral transfer. These five signatures are addressed in the following five paragraphs.

#### 5.2.1. Signature 1: Enhanced Amplitude of the Turbulence at the Shear Zone

[47] If turbulence is driven in regions of shear (tapping the energy in the flow velocities of different parcels of wind), then one would expect to see an enhanced amplitude of the turbulent fluctuations localized at the site of the driving. As can be seen in the second and third panels of Figure 11, at the stream interface where vorticity maximizes there is no enhanced level of turbulence above the statistical fluctuations in the superposed averaging. (This finding is contrary to the findings of *Bavassano and Bruno* [1989], who concluded that an increase in turbulence amplitudes is associated with shear; that conclusion was based on a comparison of two 64 h long Elsasser spectra obtained after the passage of a strong shear zone ahead of a corotating high-speed stream at 0.3 AU.) In Figure 11, there is no enhanced level of turbulence at the shear zone for measurements of the fluctuation levels with and without discontinuities and for normalized versus unnormalized fluctuations. The turbulence amplitudes in the third and fourth panels of Figure 11 can be interpreted as follows: the turbulence amplitude is low in the slow wind, the turbulence amplitude is high in the fast wind, and the turbulence amplitude increases smoothly from the lower amplitude to the higher amplitude across the CIR. No evidence for the driving of turbulence by shear is found in this examination of turbulence amplitudes.

#### 5.2.2. Signature 2: Indication in the Inward-Outward Elsasser Variables That Turbulence is More Fully Developed

[48] The solar wind tends to be dominated by fluctuations that have the nature of outward propagating Alfven waves [*Coleman*, 1966; *Belcher and Davis*, 1971; *Barnes*, 1979]. It has been argued that as the solar wind evolves there is a decay of outward traveling Alfven waves into a state where the ratio of the outward-to-inward Alfvenic fluctuations is nearer to unity [e.g., *Tu et al.*, 1990; *Roberts et al.*, 1987a; *Horbury and Schmidt*, 1999; *Goldstein and Roberts*, 1999; *Gulamali and Cargill*, 2001]. (Note, however, that a fully developed MHD turbulence need not have a balance of inward and outward fluctuations: there are models of "unbalanced" turbulence [cf. *Lithwick et al.*, 2007; *Podesta*, 2010] and supporting solar wind measurements [*Podesta et al.*, 2008, 2009]; however, the measured unbalance in the solar wind may be dominantly from strong discontinuities as demonstrated in Figure 12.) If shear in the solar wind converts the energy of outward traveling Alfven waves into a turbulent cascade by acting to scatter the Alfven waves [e.g., *Ghosh et al.*, 1998] or by generating nonlinear couplings with the Alfven waves [e.g., *Roberts et al.*, 1987a], then a change in the properties of the Elsasser amplitudes should occur abruptly at the shear. In Figure 16 (bottom) the ratio of the outward to inward power of Alfvenic fluctuations is plotted in the $4.3 \times 10^{-4} - 1.9 \times 10^{-3}$ Hz range of frequencies. The thick curve is a 13 h running average. This curve shows a smooth transition from an inward-outward near balance in the slow wind to a predominance of outward propagation in the fast wind. In the thin curve in Figure 16 (bottom) with a 1 h resolution, a signature (which may or may not be statistically significant) is seen localized about the stream interface at t = 0. This signature is a local excursion toward a dominance of outward propagation, which is opposite to the signature that the production of turbulence from outward traveling Alfven waves would give. We speculate that this enhancement could be owed to the presence of a robust tangential discontinuity at the stream interface [*González-Esparza and Smith*, 1997; *Forsyth and Marsch*, 1999], since tangential discontinuities are known to have magnetic and velocity perturbations that appear as outward traveling Alfven waves [*Neugebauer et al.*, 1984, 1986; *Neugebauer*, 1985]. In summary, in the examination of the Elsasser variables no evidence is found for the driving of turbulence by shear.

#### 5.2.3. Signature 3: Unusual Changes in the Spectra of $\delta$v and $\delta$B That Indicate Driving

[49] As noted in section 4.3, the spectral slopes of the velocity fluctuations $\delta$v and the magnetic field fluctuations $\delta$B systematically differ. This difference is not understood (however, see *Müller and Grappin* [2004, 2005]), so the expected changes in the spectral slopes at the shear zone if the shear drives turbulence are difficult to predict. If turbulence is being driven by velocity differences in shears, a change in the imbalance between the slopes of $\delta$v and $\delta$B might occur at the shear zone. As can be seen in Figure 14, there are no abrupt distinct changes in the spectral indices of $\delta$B, $\delta$v, and $\delta$E at the localized shear zone in the CIR; only a slow change across the CIR of the spread between the spectral indices of $\delta$v and $\delta$B wherein the spread is larger in the fast wind after the CIR passes than it is in the slow wind before the CIR passes. No signature of statistical significance is localized around the shear zone. To summarize, no signature of the shear zone is seen in the spectral indices of the turbulence of the solar wind.

#### 5.2.4. Signature 4: Decrease in Alfvenic Correlations Associated With Alfven-Wave Conversion

[50] If power in outward propagating Alfven waves in the solar wind is converted to a turbulence cascade in the presence of velocity shear [e.g., *Roberts et al.*, 1992; *Grappin and Velli*, 1996; *Ghosh et al.*, 1998; *Roberts and Ghosh*, 1999], then the correlation between $\delta\underline{v}$ and $\delta\underline{b}$ should diminish at the shear zone and the outward dominance of the fluctuations should diminish. These signatures would both be indicated by a reduction in the Alfvenicity at the stream interface. (Such an Alfvenicity reduction was seen in solar wind observations [*Roberts et al.*, 1992] and in the computer simulations of *Goldstein et al.* [1999].) In the first panel of Figure 13 the superposed average of the Alfvenicity $\mathcal{A}$ of the solar wind plasma is plotted as the black curves, the thin curve with 1 h resolution and the thick curve being a 7 h running average. As can be seen, there is no statistically significant decrease in the Alfvenicity coincident with the shear at the stream interface. Also in Figure 13 (bottom) no statistically significant decrease in the $\delta\underline{v}$ $\delta\underline{B}$ correlations is seen at the stream interface. Rather, at the stream interface there is an onset of temporal increase in the Alfvenicity and in the $\delta\underline{v}$ $\delta\underline{B}$ correlation that spans the compressed-fast-wind portion of the CIR. To summarize, in this examination of the Alfvenic correlations no evidence is found for the driving of turbulence by shear.

#### 5.2.5. Signature 5: A Localized Specific-Entropy Signature Associated With a Turbulence Cascade

[51] In the fifth panel of Figure 4 and in the third panel of Figure 9 the ion specific entropy of the solar wind plasma is plotted through the CIR. If turbulence is being driven by shear at the stream interface (and if the energy of spectral transfer goes into ion heating [cf. *Smith et al.*, 2001; *MacBride et al.*, 2008; *Marino et al.*, 2008; *Stawarz et al.*, 2009], then a localized increase in the ion specific entropy should be noticeable. As can be seen in Figure 9, on the slow-wind side of the stream interface the specific entropy is low, and it begins to increase strongly at the stream interface and continues its strong increase across the fast-wind side of the CIR into the fast wind. This signature appears to be a transition of the specific entropy between the slow wind and the fast wind, not a signature of turbulent heating at the stream interface. To summarize, in this examination of the specific entropy no evidence for the driving of turbulence by shear is found.

## 6. Findings

[52] The results of this study are summarized in sections 6.1–6.3. The chief findings are numbered for clarity.

### 6.1. CIR Structure

[53] Using 27 CIR events at 1 AU that had clean shear zones and that were followed by several-day-long intervals of high-speed wind, superposed-epoch analysis was performed. The zero epoch for each CIR was taken to be the CIR stream interface as determined by the maximum in the plasma vorticity.

[54] 1. Through the CIR, the mean direction of the magnetic field follows the predicted local-Parker-spiral direction.

[55] 2. When spacecraft measurements were rotated into the local-Parker-spiral coordinate system, the shear in velocity parallel to the stream interface inside the CIR was found to be abrupt. The shear-zone widths were much less than the width of the CIR itself.

[56] 3. Viewed in the local-Parker-spiral coordinate system, the large-scale convergent compressional flow perpendicular to and toward the stream interface is clearly visible. About half of the CIR events display a narrow divergent "rebound" flow away from the stream interface inside of the CIR.

[57] 4. A few properties of the plasma and turbulence exhibit smooth transitions in properties from the slow wind to the fast wind across the entire CIR: these are the amplitudes and normalized amplitudes of the velocity fluctuations and the magnetic field fluctuations. Many other parameters show strong transitions only across the compressed-fast-wind portion of the CIR: these are the specific entropy of the plasma, the ion temperature, the Alfvenicity, the absolute value of the Alfvenicity, the magnetic field spectral slope, the outward Elsasser-variable spectral slope, the inward and outward Elsasser-variable fluctuation amplitudes, and the ratio of outward-to-inward Elsasser fluctuations.

### 6.2. Turbulence Properties

[58] Analysis of velocity and magnetic field measurements from ACE provided measures of the solar wind turbulence and those measures were superpose averaged for the 27 CIR events.

[59] 1. The amplitude of the velocity and magnetic field fluctuations (with and without discontinuities in the analysis) is low in the slow wind, is high in the fast wind, and makes a smooth transition between the two levels across the CIR.

[60] 2. The Alfven ratio has similar values in the slow and fast wind: the Alfven ratio is about 0.8 if discontinuities are kept in the data set and the Alfven ratio is about 0.9 if discontinuities are excluded from the analysis. At the stream interface a sharp decrease in the Alfven ratio is seen, indicating considerably more energy in magnetic field fluctuations than in velocity fluctuations.

[61] 3. The Alfvenicity of the solar wind plasma is observed to smoothly vary from low positive values to higher positive values across the CIR from the slow wind to the fast wind. The degree of correlations between the

velocity fluctuations and the magnetic field fluctuations, as measured by the absolute value of the Alfvenicity, increases smoothly across the CIR from low values in the slow wind to higher values in the fast wind. The Alfvenicity and the degree of correlation is higher in all locations for discontinuities in the solar wind than for the solar wind plasma in general.

[62] 4. The spectral slopes of the velocity, magnetic field, and total-energy fluctuations show only weak trends across the CIR. The magnetic field spectral index is slightly shallower in the fast wind than it is in the slow wind. The total-energy spectral index is near −1.5 with the magnetic field index steeper than −1.5 and the velocity index shallower than −1.5.

[63] 5. The amplitudes of the Elsasser-variable fluctuations indicate that the slow wind is slightly dominated by outward traveling fluctuations, the slow-wind side of the CIR is slightly dominated by outward traveling fluctuations, the fast wind is strongly dominated by outward traveling fluctuations, and a smooth transition is made between the two states in the fast-wind side of the CIR. The amplitude of the inward fluctuations is similar in the slow wind and in the fast wind: the amplitude of the outward fluctuations is much higher in the fast wind than in the slow wind.

[64] 6. The spectral slopes of the inward propagating and outward propagating Elsasser variables are similar in the slow wind and in the CIR, but the spectral slope of the inward propagating variable becomes steep in the fast wind.

[65] 7. The amount of spreading of turbulence across the magnetic field in the lifetime of the solar wind plasma is limited. At 1 AU, spreading scales of $\sim 10^6$ km across the field are estimated. This spreading is much narrower than the $\sim 4 \times 10^7$ km width of a CIR at 1 AU. The limit on the spreading implies that any turbulence observed will be localized around the site where it is driven.

### 6.3. Driving of Turbulence by Shear

[66] Evidence was sought that would connect signatures that turbulence is being strongly driven at locations of strong shear in the solar wind. The strong shear regions examined were stream interfaces in CIRs at 1 AU. No such evidence was found. An assessment of five specific signatures of turbulence driving are the following: (1) An enhanced amplitude of turbulence at the stream-interface shear zone that would indicate driving of turbulence was not found. (2) No indication was found in the inward-outward Elsasser fluctuations that the turbulence is more fully developed at the stream-interface shear zone. (3) No unusual signatures in the $\delta$v and $\delta$B spectra were found at the stream-interface shear zone that would indicate a change in the driving near the shear zone. (4) No indication was found that the Alfvenicity and the Alfvenic correlations are reduced at the stream-interface shear zone. (5) No localized specific-entropy signature was found at the shear zone that would indicate enhanced ion heating by spectral transfer.

### 6.4. Future Studies

[67] A study that is a natural extension of the present study would be to compare the properties of turbulence in shear zones near the Sun with the properties of turbulence in shear zones at 1 AU. This would provide information about the temporal evolution of turbulence under shear (as compared with the temporal evolution of the unsheared solar wind). This would provide an improvement to the methodology of section 5.2 where evidence for the driving of turbulence by shear was sought via comparisons of the turbulence properties inside and outside the shear zones, all at 1 AU.

[68] A second study that is needed is a thorough examination of the effects of strong discontinuities on the fluctuation-amplitude measures and wave number spectra of the solar wind and, relatedly, spectral analysis of the solar wind between the discontinuities. And finally, an understanding of why the velocity and magnetic field spectra in the solar wind differ is needed before a full understanding of MHD turbulence can be claimed.

## Appendix A: Driving of Turbulence by Shear

[69] In this appendix, simple estimates are given as to (1) the scale sizes of the turbulence driven in a shear of a given width and (2) the time required for the turbulence cascade to fully develop when turbulence is driven in a shear.

### A1. Turbulence Spatial Scales

[70] Looking at fluid experiments and direct numerical simulations of the driving of turbulence in shear zones, one would estimate that the correlation length (large-eddy size) in the turbulence is about one half the width of the shear zone. Measurements in turbulent boundary layers find turbulence correlation lengths normal to the shear and spanwise to be about the width of the boundary layer [*Kovasznay et al.*, 1970; *Rajagopalan et al.*, 1982; *Smits et al.*, 1989], with streamwise correlations somewhat longer. Measurements in Couette flow [*Vaezi et al.*, 1997] and channel flow [*Kobayashi et al.*, 1994] find large-eddy scales in the turbulence that are about half the channel width, consistent with direct numerical simulations [e.g., *Tsukahara et al.*, 2006]. Similar results are found for measurements [*Bailey et al.*, 2008] and simulations [*Wu and Moin*, 2008] of turbulent pipe flow. And for shear zones without boundaries, the measured large-eddy scales in turbulent planar jet flow are about half of the width of the jet [*Gutmark and Wygnanski*, 1976; *Mumford*, 1982], in agreement with direct numerical simulations [*Stanley et al.*, 2002].

[71] The observed widths of the two stream-interface shear zones in Figure 7 are 2.5 h and 2.8 h (full width at half maximum of the vorticity) as seen in the OMNI2 1 h resolution data set. The width of the superposed average of the stream-interface vorticity in Figure 9 is 3.1 h and the width of the superposed average of the stream-interface vorticity in Figure 11 is 2.8 h. Such a shear layer that moves past a spacecraft at about 400 km/s with about a 45° tilt from radial that passes in 2.5 h has a width W of about $5 \times 10^6$ km.

[72] From analogy with the fluid experiments discussed above, one would expect turbulence in the stream-interface shear layer to have an integral scale (large-eddy scale) of about $W/2 = 2.5 \times 10^6$ km. This is consistent with some of the correlation lengths measured in the solar wind [e.g., *Jokipii and Coleman*, 1968; *Matthaeus and Goldstein*, 1982a; *Tu and Marsch*, 1995b; *Matthaeus et al.*, 1999; *Feynman et al.*, 1996].

[73] Note, however, that higher-time-resolution (1 min) analysis of shear in CIRs found localizations of shear layers to be narrower than the $5 \times 10^6$ km value arrived at above. *Borovsky* [2006] found concentrated shear layers with widths on the order of $1 \times 10^5$ km in CIRs; these are only some 20 times larger than the Bohm diffusion length scale for the ~100 h age of the solar wind.

### A2. Expected Cascade Development Time Scales

[74] In Kolmogorov fluid turbulence, the time scale for spectral transfer from large-scale fluctuations toward smaller scales is the eddy-turnover time $\tau_{eddy}$ (e.g., section 3.2 of *Tennekes and Lumley* [1972] and section 7.2 of *Frisch* [1995]): every local eddy-turnover time, the fluctuation energy is transferred to spatial scales a factor of 2 smaller. The eddy-turnover time in a Kolmogorov turbulence spectrum varies with wave number k as $\tau_{eddy} \propto k^{-2/3}$ [e.g., *Frisch*, 1995, equation (7.2)]. Starting from the integral scale $k_o$, the Kolmogorov cascade will propagate to infinitely higher k in a time scale that is 2.7 times the integral-scale eddy-turnover time. (The factor 2.7 is the sum of the geometric series obtained by adding up the k-dependent eddy-turnover times for the factor of 2 increases in k.) For a Kraichnan spectrum of turbulence where the eddy-turnover time scales with wave number k as $\tau_{eddy} \propto k^{-1/2}$ [e.g., *Borovsky and Gary*, 2009, equation (9)] the sum of the geometric series yields a numerical factor of 3.41. Hence the Kraichnan spectrum will fully develop in 3.41 integral-scale eddy-turnover times.

[75] The eddy-turnover time teddy is defined as $\tau_{eddy} = L_{eddy}/\delta v$, where $L_{eddy}$ is the diameter of the eddy and $\delta v$ is the velocity shear across the eddy. For a large eddy driven by the stream-interface velocity shear $\omega = dv/dx$, the velocity $\delta v$ across the eddy would be approximately $\delta v = L_{eddy}(dv/dx) = \omega L_{eddy}$. With this last relation, the eddy-turnover time $\tau_{eddy} = L_{eddy}/\delta v$ for an eddy driven by the shear is $\tau_{eddy} = \omega^{-1}$, independent of the eddy size. In Figures 7, 9, and 11 it is seen that the peak vorticity in the stream-interface shear zone is $\omega = 5 \times 10^{-5}$ s$^{-1}$, and the mean vorticity in the shear zone is about $2.5 \times 10^{-5}$ s$^{-1}$. This mean vorticity gives a large-eddy eddy-turnover time $\tau_{eddy} = \omega^{-1} = 11.1$ h. Taking 2.7 (Kolmogorov) to 3.4 (Kraichnan) times $\tau_{eddy}$ for the cascade-development time yields 30–38 h for the full development of the turbulence cascade.

[76] Note that closer to the Sun than 1 AU the vorticity at the stream interface should be higher than the values of Figures 7, 9, and 11. For instance, at 0.3 AU the transverse expansion of the solar wind is less than it is at 1 AU, even in a CIR compression region, which is really a weakened expansion [cf. *Hundhausen*, 1973, Figure 4]. With the velocity change preserved and the width of the shear zone decreased by a factor of approximately 0.3/1.0, the vorticity at 0.3 AU would be increased by a factor of 1.0/0.3 = 3.3, which reduces the cascade-formation time at 0.3 AU by a factor of 3.3 to a time on the order of 10 h.

[77] Note also that CIR shear zones show enhanced localized vorticity when examined with higher-time-resolution measurements. *Borovsky* [2006] (compare Figure 12) observed vorticities in CIRs an order of magnitude higher than the $\omega = 5 \times 10^{-5}$ s$^{-1}$ value being discussed here, which would lead to faster development of turbulence cascades but at shorter wave numbers. To summarize this appendix, the length scales of the turbulence expected to be driven by CIR stream-interface shear zones should have spatial scales of ~$2.5 \times 10^{-6}$ km and smaller, with a fully developed turbulence spectrum at 1 AU.

[78] **Acknowledgments.** The authors wish to thank Joachim Birn, Jack Gosling, John Podesta, Pete Riley, Ruth Skoug, and John Steinberg for helpful conversations. This research was supported by the NASA Heliospheric SR&T Program, by the NASA Heliospheric Guest-Investigator Program, by the NSF SHINE Program, and by the LDRD Program at Los Alamos National Laboratory. Work at Lancaster University was supported under STFC grant SBA7743.

[79] Philippa Browning thanks Melvyn Goldstein and another reviewer for their assistance in evaluating this paper.

## References

Alevizos, A., J. Plygiannakis, A. Kakouris, and X. Moussas (1999), A method for spherical harmonic analysis of Comton-Getting corrected 3-D energetic particle distributions, *Sol. Phys.*, *186*, 401, doi:10.1023/A:1005145021168.

Alexakis, A., P. E. Mininni, and A. Pouquet (2005), Shell-to-shell energy transfer in magnetohydrodynamics: I. Steady state turbulence, *Phys. Rev. E*, *72*, 046301, doi:10.1103/PhysRevE.72.046301.

Alfven, H., and C.-G. Falthammar (1963), *Cosmical Electrodynamics*, sect. 3.6, Oxford Univ. Press, London.

Ashforth-Frost, S., K. Jambunathan, and C. F. Whitney (1997), Velocity and turbulence characteristics of a semiconfined orthogonally impinging slot jet, *Exp. Therm. Fluid Sci.*, *14*, 60, doi:10.1016/S0894-1777(96)00112-4.

Bailey, S. C. C., M. Hultmark, A. J. Smits, and M. P. Schultz (2008), Azimuthal structure of turbulence in high Reynolds number pipe flow, *J. Fluid Mech.*, *615*, 121, doi:10.1017/S0022112008003492.

Bame, S. J., J. R. Asbridge, W. C. Feldman, J. T. Gosling, and R. D. Zwickl (1981), Bi-directional streaming of solar wind electrons >80 eV: ISEE evidence for a closed-field structure within the driver gas of an interplanetary shock, *Geophys. Res. Lett.*, *8*, 173, doi:10.1029/GL008i002p00173.

Barnes, A. (1979), Hydromagnetic waves and turbulence in the solar wind, in *Solar System Plasma Physics*, vol. 1, edited by E. N. Parker, C. F. Kennel, and L. J. Lanzerotti, pp. 249–319, North Holland, Amsterdam.

Bartley, W. C., R. P. Bakata, K. G. McCracken, and U. R. Rao (1966), Anisotropic cosmic radiation fluxes of solar origin, *J. Geophys. Res.*, *71*, 3297.

Bavassano, B., and R. Bruno (1989), Evidence of local generation of Alfvenic turbulence in the solar wind, *J. Geophys. Res.*, *94*, 11,977, doi:10.1029/JA094iA09p11977.

Bavassano, B., and R. Bruno (1992), On the role of interplanetary sources in the evolution of low-frequency Alfvenic turbulence in the solar wind, *J. Geophys. Res.*, *97*, 19,129, doi:10.1029/92JA01510.

Belcher, J. W., and L. Davis (1971), Large-amplitude Alfven waves in the interplanetary medium, 2, *J. Geophys. Res.*, *76*, 3534, doi:10.1029/JA076i016p03534.

Belcher, J. W., and C. V. Solodyna (1975), Alfven waves and directional discontinuities in the interplanetary medium, *J. Geophys. Res.*, *80*, 181, doi:10.1029/JA080i001p00181.

Bhattacharjee, A., C. S. Ng, and S. R. Spangler (1998), Weakly compressive MHD turbulence in the solar wind and the interstellar medium, *Astrophys. J.*, *494*, 409, doi:10.1086/305184.

Bieber, J. W., J. Chen, W. H. Matthaeus, C. W. Smith, and M. A. Pomerantz (1993), Long-term variations of interplanetary magnetic field spectra with implications for cosmic ray modulation, *J. Geophys. Res.*, *98*, 3585, doi:10.1029/92JA02566.

Boldyrev, S. (2006), Spectrum of magnetohydrodynamic turbulence, *Phys. Rev. Lett.*, *96*, 115002, doi:10.1103/PhysRevLett.96.115002.

Borg, G. G., M. H. Brennan, R. C. Cross, L. Giannone, and I. J. Donnelly (1985), Guided propagation of Alfven waves in a toroidal plasma, *Plasma Phys. Controlled Fusion*, *27*, 1125, doi:10.1088/0741-3335/27/10/004.

Borovsky, J. E. (2006), The eddy viscosity and flow properties of the solar wind: CIRs, CME sheaths, and solar-wind/magnetosphere coupling, *Phys. Plasmas*, *13*, 056505, doi:10.1063/1.2200308.

Borovsky, J. E. (2008), The flux-tube texture of the solar wind: Strands of the magnetic carpet at 1 AU?, *J. Geophys. Res.*, *113*, A08110, doi:10.1029/2007JA012684.

Borovsky, J. E. (2010), On the variations of the solar-wind magnetic field about the Parker-spiral direction, *J. Geophys. Res.*, *115*, A09101, doi:10.1029/2009JA015040.

Borovsky, J. E., and M. H. Denton (2009), Relativistic-electron dropouts and recovery: A superposed epoch study of the magnetosphere and the solar wind, *J. Geophys. Res.*, *114*, A02201, doi:10.1029/2008JA013128.

Borovsky, J. E., and H. O. Funsten (2003a), MHD turbulence in the Earth's plasma sheet: Dynamics, dissipation, and driving, *J. Geophys. Res.*, *108*(A7), 1284, doi:10.1029/2002JA009625.

Borovsky, J. E., and H. O. Funsten (2003b), Role of solar wind turbulence in the coupling of the solar wind to the Earth's magnetosphere, *J. Geophys. Res.*, *108*(A6), 1246, doi:10.1029/2002JA009601.

Borovsky, J. E., and S. P. Gary (2009), On viscosity and the Reynolds number of MHD turbulence in collisionless plasmas: Coulomb collisions, Landau damping, and Bohm diffusion, *Phys. Plasmas*, *16*, 082307, doi:10.1063/1.3155134.

Borovsky, J. E., and J. T. Steinberg (2006a), The freestream turbulence effect in solar-wind/magnetosphere coupling: Analysis through the solar cycle and for various types of solar wind, in *Recurrent Magnetic Storms: Corotating Solar Wind Streams*, *Geophys. Monogr. Ser.*, vol. 167, edited by B. Tsurutani et al., pp. 59–76, AGU, Washington, D.C.

Borovsky, J. E., and J. T. Steinberg (2006b), The "calm before the storm" in CIR/magnetosphere interactions: Occurrence statistics, solar-wind statistics, and magnetospheric preconditioning, *J. Geophys. Res.*, *111*, A07S10, doi:10.1029/2005JA011397.

Borovsky, J. E., R. C. Elphic, H. O. Funsten, and M. F. Thomsen (1997), The Earth's plasma sheet as a laboratory for flow turbulence in high-beta MHD, *J. Plasma Phys.*, *57*, 1, doi:10.1017/S0022377896005259.

Borovsky, J. E., M. F. Thomsen, and R. C. Elphic (1998), The driving of the plasma sheet by the solar wind, *J. Geophys. Res.*, *103*, 17,617, doi:10.1029/97JA02986.

Borrini, G., J. T. Gosling, S. J. Bame, W. C. Feldman, and J. M. Wilcox (1981), Solar wind helium and hydrogen structure near the heliospheric current sheet: A signal of coronal streamers at 1 AU, *J. Geophys. Res.*, *86*, 4565, doi:10.1029/JA086iA06p04565.

Branover, H., A. Eidelman, E. Golbraikh, A. Kapusta, and B. Mikhailovich (2004), Wave-mean flow interaction in an MHD wake behind a body, *Fluid Dyn. Res.*, *35*, 287, doi:10.1016/j.fluiddyn.2004.07.001.

Bruno, R. (1997), Observations of MHD turbulence in the solar wind, *Nuovo Cimento Soc. Ital. Fis. C*, *20*, 881.

Bruno, R., and V. Carbone (2005), The solar wind as a turbulence laboratory, *Living Rev. Sol. Phys.*, *2*, lrsp-2005-2.

Bruno, R., V. Carbone, P. Veltri, E. Pietropaolo, and B. Bavassano (2001), Identifying intermittency events in the solar wind, *Planet. Space Sci.*, *49*, 1201, doi:10.1016/S0032-0633(01)00061-7.

Burlaga, L. F. (1968), Micro-scale structures in the interplanetary medium, *Sol. Phys.*, *4*, 67, doi:10.1007/BF00146999.

Burlaga, L. F. (1969), Directional discontinuities in the interplanetary magnetic field, *Sol. Phys.*, *7*, 54, doi:10.1007/BF00148406.

Burlaga, L. F., and R. P. Lepping (1977), The causes of recurrent geomagnetic storms, *Planet. Space Sci.*, *25*, 1151, doi:10.1016/0032-0633(77)90090-3.

Burlaga, L. F., and N. F. Ness (1997), Global patterns of heliospheric magnetic field polarities and elevation angles: 1990 through 1995, *J. Geophys. Res.*, *102*, 19,731, doi:10.1029/97JA01568.

Burlaga, L. F., R. P. Lepping, K. W. Behannon, L. W. Klien, and F. M. Neubauer (1982), Large-scale variations of the interplanetary magnetic field: Voyager 1 and 2 observations between 1–5 AU, *J. Geophys. Res.*, *87*, 4345, doi:10.1029/JA087iA06p04345.

Burlaga, L. F., W. H. Mish, and Y. C. Whang (1990), Coalescence of recurrent streams of different sizes and amplitudes, *J. Geophys. Res.*, *95*, 4247, doi:10.1029/JA095iA04p04247.

Carbone, V. (1993), The inertial-range spectrum of fully developed magnetohydrodynamic turbulence, *Ann. Geophys.*, *11*, 866.

Carbone, V., F. Malara, and P. Veltri (1992), Anisotropy in the spectra of Alfvenic MHD fluctuations in the solar wind, in *Solar Wind Seven*, edited by E. Marsch and R. Schwenn, pp. 433–436, Pergamon, New York.

Cattaneo, F. (1994), On the effects of a weak magnetic field on turbulent transport, *Astrophys. J.*, *434*, 200, doi:10.1086/174717.

Chen, H., and D. Montgomery (1987), Turbulent MHD transport coefficients: An attempt at self-consistency, *Plasma Phys. Controlled Fusion*, *29*, 205, doi:10.1088/0741-3335/29/2/006.

Cho, J., and A. Lazarian (2005), Generation of compressible modes in MHD turbulence, *Theor. Comput. Fluid Dyn.*, *19*, 127, doi:10.1007/s00162-004-0157-x.

Cho, J., and E. T. Vishniac (2000), The anisotropy of magnetohydrodynamic Alfvenic turbulence, *Astrophys. J.*, *539*, 273, doi:10.1086/309213.

Clack, D., R. J. Forsyth, and M. W. Dunlop (2000), Ulysses observations of the magnetic field structure within CIRs, *Geophys. Res. Lett.*, *27*, 625, doi:10.1029/1999GL010764.

Coleman, P. J. (1966), Hydromagnetic waves in the interplanetary plasma, *Phys. Rev. Lett.*, *17*, 207, doi:10.1103/PhysRevLett.17.207.

Coleman, P. J. (1968), Turbulence, viscosity, and dissipation in the solar-wind plasma, *Astrophys. J.*, *153*, 371, doi:10.1086/149674.

Cooley, J. W., and J. W. Tukey (1965), An algorithm for the machine calculation of complex Fourier series, *Math. Comput.*, *19*, 297, doi:10.2307/2003354.

Cranmer, S. R. (2008), Turbulence-driven polar winds from T Tauri stars energized by magnetospheric accretion, *Astrophys. J.*, *689*, 316, doi:10.1086/592566.

Crooker, N. U., and J. T. Gosling (1999), CIR morphology, turbulence, discontinuities, and energetic particles, *Space Sci. Rev.*, *89*, 179, doi:10.1023/A:1005253526438.

Debliquy, O., M. K. Verma, and D. Carati (2005), Energy fluxes and shell-to-shell transfers in three-dimensional decaying magnetohydrodynamic turbulence, *Phys. Plasmas*, *12*, 042309, doi:10.1063/1.1867996.

Denton, M. H., and J. E. Borovsky (2008), Superposed epoch analysis of high-speed-stream effects at geosynchronous orbit: Hot plasma, cold plasma, and the solar wind, *J. Geophys. Res.*, *113*, A07216, doi:10.1029/2007JA012998.

Denton, M. H., and J. E. Borovsky (2009), The superdense plasma sheet in the magnetosphere during high-speed-steam-driven storms: Plasma transport timescales, *J. Atmos. Sol. Terr. Phys.*, *71*, 1045, doi:10.1016/j.jastp.2008.04.023.

Denton, M. H., J. E. Borovsky, and T. E. Cayton (2010), A density-temperature description of the outer electron radiation belt during geomagnetic storms, *J. Geophys. Res.*, *115*, A01208, doi:10.1029/2009JA014183.

Dobrowolny, M., A. Mangeney, and P. L. Veltri (1980), Properties of magnetohydrodynamic turbulence in the solar wind, in *Solar and Interplanetary Dynamics*, edited by M. Dryer and E. Tandberg-Hanssen, pp. 143–146, Int. Astron. Union, Riedel, Dordrecht, The Netherlands.

Douglas, J., E. Kim, and A. Thyagaraja (2008), Effects of flow shear and Alfven waves on two-dimensional magnetohydrodynamic turbulence, *Phys. Plasmas*, *15*, 052301, doi:10.1063/1.2913270.

Drell, S. D., H. M. Foley, and M. A. Ruderman (1965), Drag and propulsion of large satellite in the ionosphere: An Alfven propulsion engine in space, *J. Geophys. Res.*, *70*, 3131, doi:10.1029/JZ070i013p03131.

Elliott, H. A., D. J. McComas, N. A. Schwadron, J. T. Gosling, R. M. Skoug, G. Gloeckler, and T. H. Zurbuchen (2005), An improved expected temperature formula for identifying ICMEs, *J. Geophys. Res.*, *110*, A04103, doi:10.1029/2004JA010794.

Fejer, J. A., and K. F. Lee (1967), Guided propagation of Alfven waves in the magnetosphere, *J. Plasma Phys.*, *1*, 387, doi:10.1017/S0022377800003408.

Feldman, W. C., J. R. Asbridge, S. J. Bame, J. T. Gosling, and D. S. Lemons (1978), Characteristic electron variations across simple high-speed solar wind streams, *J. Geophys. Res.*, *83*, 5285, doi:10.1029/JA083iA11p05285.

Feynman, J., A. A. Ruzmaikin, and E. J. Smith (1996), Radial evolution of the high/low frequency breakpoint in magnetic field spectra, AIP Conf. Proc., 382, 347.

Forsyth, R. J., and E. Marsch (1999), Solar origin and interplanetary evolution of stream interfaces, *Space Sci. Rev.*, *89*, 7, doi:10.1023/A:1005235626013.

Frank, M., L. Barleon, and U. Muller (2001), Visual analysis of two-dimensional magnetohydrodynamics, *Phys. Plasmas*, *13*, 2287.

Frisch, U. (1995), *Turbulence*, Cambridge Univ. Press, New York.

Fyfe, D., D. Montgomery, and G. Joyce (1977), Dissipative, forced turbulence in two-dimensional magnetohydrodynamics, *J. Plasma Phys.*, *17*, 369, doi:10.1017/S0022377800020687.

Gary, S. P. (1993), *Theory of Space Plasma Microinstabilities*, sect. 6.2.1, Cambridge Univ. Press, New York.

Gazis, P. R. (1984), Observations of plasma bulk parameters and energy balance of the solar wind between 1 and 10 AU, *J. Geophys. Res.*, *89*, 775, doi:10.1029/JA089iA02p00775.

Ghosh, S., and M. L. Goldstein (1997), Anisotropy in Hall MHD turbulence due to a mean magnetic field, *J. Plasma Phys.*, *57*, 129, doi:10.1017/S0022377896005260.

Ghosh, S., W. H. Matthaeus, D. A. Roberts, and M. L. Goldstein (1998), The evolution of slab fluctuations in the presence of pressure-balanced magnetic structures and velocity shears, *J. Geophys. Res.*, *103*, 23,691, doi:10.1029/98JA02195.

Goertz, C. K., and R. W. Boswell (1979), Magnetosphere-ionosphere coupling, *J. Geophys. Res.*, *84*, 7239, doi:10.1029/JA084iA12p07239.

Goldreich, P., and S. Sridhar (1997), Magnetohydrodynamic turbulence revisited, *Astrophys. J.*, *485*, 680, doi:10.1086/304442.

Goldstein, M. L. (2001), Major unsolved problems in space plasma physics, *Astrophys. Space Sci.*, *277*, 349, doi:10.1023/A:1012264131485.

Goldstein, M. L., and D. A. Roberts (1999), Magnetohydrodynamic turbulence in the solar wind, *Phys. Plasmas*, *6*, 4154, doi:10.1063/1.873680.

Goldstein, M. L., D. A. Roberts, and W. H. Matthaeus (1995), Magnetohydrodynamic turbulence in the solar wind, *Annu. Rev. Astron. Astrophys.*, *33*, 283, doi:10.1146/annurev.aa.33.090195.001435.

Goldstein, M. L., D. A. Roberts, A. E. Deane, S. Ghosh, and H. K. Wong (1999), Numerical simulation of Alfvenic turbulence in the solar wind, *J. Geophys. Res.*, *104*, 14,437, doi:10.1029/1998JA900128.

Gomez, T., H. Politano, and A. Pouquet (1999), On the validity of a nonlocal approach for MHD turbulence, *Phys. Fluids*, *11*, 2298, doi:10.1063/1.870092.

González-Esparza, J. A., and E. J. Smith (1997), Three-dimensional nature of interaction regions: Pioneer, Voyager, and Ulysses solar cycle variations from 1 to 5 AU, *J. Geophys. Res.*, *102*, 9781, doi:10.1029/97JA00516.

Gosling, J. T., and V. J. Pizzo (1999), Formation and evolution of corotating interaction regions and their three dimensional structure, *Space Sci. Rev.*, *89*, 21, doi:10.1023/A:1005291711900.

Gosling, J. T., V. Pizzo, and S. J. Bame (1973), Anomalously low proton temperatures in the solar wind following interplanetary shock waves: Evidence for magnetic bottles?, *J. Geophys. Res.*, *78*, 2001, doi:10.1029/JA078i013p02001.

Gosling, J. T., J. R. Asbridge, S. J. Bame, and W. C. Feldman (1978), Solar wind stream interfaces, *J. Geophys. Res.*, *83*, 1401, doi:10.1029/JA083iA04p01401.

Gosling, J. T., G. Borrini, J. R. Asbridge, S. J. Bame, W. C. Feldman, and R. T. Hansen (1981), Coronal streamers in the solar wind at 1 AU, *J. Geophys. Res.*, *86*, 5438, doi:10.1029/JA086iA07p05438.

Gosling, J. T., D. N. Baker, S. J. Bame, W. C. Feldman, R. D. Zwickl, and E. J. Smith (1987), Bidirectional solar wind electron heat flux events, *J. Geophys. Res.*, *92*, 8519, doi:10.1029/JA092iA08p08519.

Grappin, R., and M. Velli (1996), Waves and streams in the expanding solar wind, *J. Geophys. Res.*, *101*, 425, doi:10.1029/95JA02147.

Grappin, R., A. Mangeney, and E. Marsch (1990), On the origin of solar wind MHD turbulence: Helios data revisited, *J. Geophys. Res.*, *95*, 8197, doi:10.1029/JA095iA06p08197.

Gulamali, M. Y., and P. J. Cargill (2001), Ulysses observations of magnetohydrodynamic turbulence in corotating interaction regions, *J. Geophys. Res.*, *106*, 15,687, doi:10.1029/2000JA000390.

Gutmark, E., and I. Wygnanski (1976), The planar turbulent jet, *J. Fluid Mech.*, *73*, 465, doi:10.1017/S0022112076001468.

Horbury, T. S., and J. M. Schmidt (1999), Development and effects of turbulence in connection with CIRs, *Space Sci. Rev.*, *89*, 61, doi:10.1023/A:1005260331464.

Humphreys, J. S. (1960), On a circular cylinder in a steady wind at transition Reynolds number, *J. Fluid Mech.*, *9*, 603, doi:10.1017/S0022112060001341.

Hundhausen, A. J. (1973), Nonlinear model of high-speed solar wind streams, *J. Geophys. Res.*, *78*, 1528, doi:10.1029/JA078i010p01528.

Ilie, R., M. W. Liemohn, M. F. Thomsen, J. E. Borovsky, and J. Zhang (2008), Influence of epoch time selection on the results of superposed epoch analysis using ACE and MPA data, *J. Geophys. Res.*, *113*, A00A14, doi:10.1029/2008JA013241.

Intriligator, D. S., J. R. Jokipii, T. S. Horbury, J. M. Intriligator, R. J. Forsyth, H. Kunow, G. Wibberenz, and J. T. Gosling (2001), Processes associated with particle transport in corotating interaction regions and near stream interfaces, *J. Geophys. Res.*, *106*, 10,625, doi:10.1029/2000JA000070.

Ishizawa, A., and Y. Hattori (1998), Large coherent structure formation by magnetic stretching term in two-dimensional MHD turbulence, *J. Phys. Soc. Jpn.*, *67*, 4302, doi:10.1143/JPSJ.67.4302.

Jokipii, J. R., and P. J. Coleman (1968), Cosmic-ray diffusion tensor and its variation observed with Mariner 4, *J. Geophys. Res.*, *73*, 5495, doi:10.1029/JA073i017p05495.

Jones, G. H., A. Balogh, and R. J. Forsyth (1998), Radial heliospheric magnetic fields detected by Ulysses, *Geophys. Res. Lett.*, *25*, 3109, doi:10.1029/98GL52259.

Kim, E., T. S. Hahm, and P. H. Diamond (2001), Eddy viscosity and laminarization of sheared flow in three dimensional reduced magnetohydrodynamic turbulence, *Phys. Plasmas*, *8*, 3576, doi:10.1063/1.1383284.

King, J. H., and N. E. Papitashvili (2005), Solar wind spatial scales in and comparisons of hourly Wind and ACE plasma and magnetic field data, *J. Geophys. Res.*, *110*, A02104, doi:10.1029/2004JA010649.

Klein, L., R. Bruno, B. Bavassano, and H. Rosenbauer (1993), Anisotropy and minimum variance of magnetohydrodynamic fluctuations in the inner heliosphere, *J. Geophys. Res.*, *98*, 17,461, doi:10.1029/93JA01522.

Kobayashi, M., H. Maekawa, Y. Shimizu, and K. Uchiyama (1994), Experimental study on turbulent flow in two-dimensional curved channel, *JSME Int. J., Ser. B*, *37*, 38.

Kovasznay, L. S. G., V. Kibens, and R. F. Backwelder (1970), Large-scale motion of the intermittent region of a turbulent boundary layer, *J. Fluid Mech.*, *41*, 283, doi:10.1017/S0022112070000629.

Kraichnan, R. H. (1965), Inertial-range spectrum of hydromagnetic turbulence, *Phys. Fluids*, *8*, 1385, doi:10.1063/1.1761412.

Kuranz, C. C., et al. (2005), Progress toward the study of laboratory scale, astrophysically relevant, turbulent plasmas, *Astrophys. Space Sci.*, *298*, 9, doi:10.1007/s10509-005-3906-4.

Lazarus, A., J. Kasper, A. Szabo, and K. Ogilvie (2003), Solar wind streams and their origins, *AIP Conf. Proc.*, *679*, 187.

Leneman, D., W. Gekelman, and J. Maggs (1999), Laboratory observations of shear Alfven waves launched from a small source, *Phys. Rev. Lett.*, *82*, 2673, doi:10.1103/PhysRevLett.82.2673.

Li, G. (2007), Flux tubes in the fast and slow solar wind, *AIP Conf. Proc.*, *932*, 26.

Lithwick, Y., and P. Goldreich (2003), Imbalanced weak magnetohydrodynamic turbulence, *Astrophys. J.*, *582*, 1220, doi:10.1086/344676.

Lithwick, Y., P. Goldreich, and S. Sridhar (2007), Imbalanced strong MHD turbulence, *Astrophys. J.*, *655*, 269.

Lopez, R. E. (1987), Solar cycle invariance in solar wind proton temperature relationships, *J. Geophys. Res.*, *92*, 11,189, doi:10.1029/JA092iA10p11189.

Lucek, E. A., and A. Balogh (1998), The identification and characterization of Alfvenic fluctuations in Ulysses data at midlatitudes, *Astrophys. J.*, *507*, 984, doi:10.1086/306372.

Lucek, E. A., D. Constantinescu, M. L. Goldstein, J. Pickett, J. L. Pincon, F. Sahraoui, R. A. Treumann, and S. N. Walker (2005), The magnetosheath, *Space Sci. Rev.*, *118*, 95, doi:10.1007/s11214-005-3825-2.

MacBride, B. T., C. W. Smith, and M. A. Forman (2008), The turbulent cascade at 1 AU: Energy transfer and the third-order scaling for MHD, *Astrophys. J.*, *679*, 1644, doi:10.1086/529575.

Malara, F., P. Veltri, and L. Primavera (1997), Nature of the density–magnetic-field-intensity correlation observed in the solar wind, *Phys. Rev. E*, *56*, 3508, doi:10.1103/PhysRevE.56.3508.

Mariani, F., B. Bavassano, U. Villante, and N. F. Ness (1973), Variations of the occurrence rate of discontinuities in the interplanetary magnetic field, *J. Geophys. Res.*, *78*, 8011, doi:10.1029/JA078i034p08011.

Marino, R., L. Sorriso-Valvo, V. Carbone, A. Noullez, R. Bruno, and B. Bavassano (2008), Heating the solar wind by a magnetohydrodynamic turbulent energy cascade, *Astrophys. J.*, *677*, L71, doi:10.1086/587957.

Marsch, E. (1991), *Physics of the Inner Heliosphere II*, edited by R. Schwenn and E. Marsch, sect. 10.2.2, pp. 159–241, Springer, Berlin.

Matthaeus, W. H., and M. L. Goldstein (1982a), Measurement of the rugged invariants of magnetohydrodynamic turbulence in the solar wind, *J. Geophys. Res.*, *87*, 6011, doi:10.1029/JA087iA08p06011.

Matthaeus, W. H., and M. L. Goldstein (1982b), Stationarity of magnetohydrodynamical fluctuations in the solar wind, *J. Geophys. Res.*, *87*, 10,347, doi:10.1029/JA087iA12p10347.

Matthaeus, W. H., and Y. Zhou (1989), Extended inertial range phenomenology of magnetohydrodynamic turbulence, *Phys. Fluids B*, *1*, 1929.

Matthaeus, W. H., M. L. Goldstein, and J. H. King (1986), An interplanetary magnetic field ensemble at 1 AU, *J. Geophys. Res.*, *91*, 59, doi:10.1029/JA091iA01p00059.

Matthaeus, W. H., S. Ghosh, S. Oughton, and D. A. Roberts (1996), Anisotropic three-dimensional MHD turbulence, *J. Geophys. Res.*, *101*, 7619, doi:10.1029/95JA03830.

Matthaeus, W. H., C. W. Smith, and S. Oughton (1998), Dynamical age of solar wind turbulence in the outer heliosphere, *J. Geophys. Res.*, *103*, 6495, doi:10.1029/97JA03729.

Matthaeus, W. H., C. W. Smith, and J. W. Bieber (1999), Correlation lengths, the ultrascale, and the spatial structure of interplanetary turbulence, *AIP Conf. Proc.*, *471*, 511.

Matthaeus, W. H., S. Dasso, J. M. Weygand, L. J. Milano, C. W. Smith, and M. G. Kivelson (2005), Spatial correlation of solar-wind turbulence from two-point measurements, *Phys. Rev. Lett.*, *95*, 231101.

Matthaeus, W. H., A. Pouquet, P. D. Mininni, P. Dmitruk, and B. Breech (2008), Rapid alignment of velocity and magnetic field in magnetohydrodynamic turbulence, *Phys. Rev. Lett.*, *100*, 085003, doi:10.1103/PhysRevLett.100.085003.

McComas, D. J., S. J. Blame, P. Barker, W. C. Feldman, J. L. Phillips, P. Riley, and J. W. Griffee (1998), Solar Wind Electron Proton Alpha Monitor (SWEPAM) for the Advanced Composition Explorer, *Space Sci. Rev.*, *86*, 563, doi:10.1023/A:1005040232597.

McCracken, K. G., and N. F. Ness (1966), The collimation of cosmic rays by the interplanetary magnetic field, *J. Geophys. Res.*, *71*, 3315.

McPherron, R. L., and J. Weygand (2006), The solar wind and geomagnetic activity as a function of time relative to corotating interaction regions, in *Recurrent Magnetic Storms: Corotating Solar Wind Streams*, *Geophys. Monogr. Ser.*, vol. 167, edited by B. Tsurutani et al., p. 125, AGU, Washington, D.C.

Mikhailovskii, A. B., J. G. Lominadze, A. P. Churikov, V. D. Pustovitov, N. N. Erokhin, and S. V. Konovalov (2008), Kinetic theory of instabilities

responsible for magnetic turbulence in laboratory rotating plasma, *Phys. Lett. A*, *372*, 3846, doi:10.1016/j.physleta.2008.02.052.
Milano, L. J., W. H. Matthaeus, P. Dmitruk, and D. C. Montgomery (2001), Local anisotropy in incompressible magnetohydrodynamic turbulence, *Phys. Plasmas*, *8*, 2673, doi:10.1063/1.1369658.
Mininni, P. D., Y. Ponty, D. C. Montgomery, J.-F. Pinton, H. Politano, and A. Pouquet (2005a), Dynamo regimes with a nonhelical forcing, *Astrophys. J.*, *626*, 853, doi:10.1086/429911.
Mininni, P. D., A. Alexakis, and A. Pouquet (2005b), Shell to shell energy transfer in MHD, Part II: Kinematic dynamo, *Phys. Rev. E*, *72*, 046302, doi:10.1103/PhysRevE.72.046302.
Montgomery, D., and L. Turner (1981), Anisotropic magnetohydrodynamic turbulence in a strong external magnetic field, *Phys. Fluids*, *24*, 825, doi:10.1063/1.863455.
Morales, G. J., and J. E. Maggs (1997), Structure of kinetic Alfven waves with small transverse scale length, *Phys. Plasmas*, *4*, 4118, doi:10.1063/1.872531.
Müller, W.-C., and D. Biskamp (2000), Scaling properties of three-dimensional magnetohydrodynamic turbulence, *Phys. Rev. Lett.*, *84*, 475, doi:10.1103/PhysRevLett.84.475.
Müller, W.-C., and R. Grappin (2004), The residual energy in freely decaying magnetohydrodynamic turbulence, *Plasma Phys. Controlled Fusion*, *46*, B91, doi:10.1088/0741-3335/46/12B/008.
Müller, W.-C., and R. Grappin (2005), Spectral energy dynamics in magnetohydrodynamic turbulence, *Phys. Rev. Lett.*, *95*, 114502, doi:10.1103/PhysRevLett.95.114502.
Mumford, J. C. (1982), The structure of the large eddies in fully developed turbulent shear flows. Part 1. The plane jet, *J. Fluid Mech.*, *118*, 241, doi:10.1017/S0022112082001062.
Murphy, N., E. J. Smith, and N. A. Schwadron (2002), Strongly underwound magnetic fields in co-rotating rarefaction regions: Observations and implications, *Geophys. Res. Lett.*, *29*(22), 2066, doi:10.1029/2002GL015164.
Ness, N. F., and J. M. Wilcox (1966), Extension of the photospheric magnetic field into interplanetary space, *Astrophys. J.*, *143*, 23, doi:10.1086/148473.
Ness, N. F., C. S. Scearce, and S. Cantarano (1966), Preliminary results for the Pioneer 6 magnetic field experiment, *J. Geophys. Res.*, *71*, 3305.
Neugebauer, M. (1985), Alignment of velocity and field changes across tangential discontinuities in the solar wind, *J. Geophys. Res.*, *90*, 6627, doi:10.1029/JA090iA07p06627.
Neugebauer, M., D. R. Clay, B. E. Goldstein, B. T. Tsurutani, and R. D. Zwickl (1984), A reexamination of rotational and tangential discontinuities in the solar wind, *J. Geophys. Res.*, *89*, 5395, doi:10.1029/JA089iA07p05395.
Neugebauer, M., C. J. Alexander, R. Schwenn, and A. K. Richter (1986), Tangential discontinuities in the solar wind: Correlated field and velocity changes and the Kelvin-Helmholz instability, *J. Geophys. Res.*, *91*, 13,694, doi:10.1029/JA091iA12p13694.
Neugebauer, M., B. E. Goldstein, D. J. McComas, S. T. Suess, and A. Balogh (1995), Ulysses observations of microstreams in the solar wind from coronal holes, *J. Geophys. Res.*, *100*, 23,389, doi:10.1029/95JA02723.
Neugebauer, M., A. Ruzmaikin, and D. J. McComas (1997), Wavelet analysis of the structure of microstreams in the polar solar wind, *AIP Conf. Proc.*, *385*, 41.
Newton, A. P. L., and E. Kim (2009), Investigation into the dual role of shear flow in 2D MHD turbulence, *Phys. Rev. Lett.*, *102*, 165002, doi:10.1103/PhysRevLett.102.165002.
Otnes, R. K., and L. Enochson (1972), *Digital Time Series Analysis*, chap. 5 and 6, pp. 197–278, John Wiley, New York.
Oughton, S. (2003), Solar wind fluctuations: Waves and turbulence, in *Solar Wind Ten*, edited by M. Velli, R. Bruno, and F. Malara, pp. 421–426, Am. Inst. of Phys., College Park, Md.
Oughton, S., W. H. Matthaeus, and S. Ghosh (1998), Scaling of spectral anisotropy with magnetic field strength in decaying magnetohydrodynamic turbulence, *Phys. Plasmas*, *5*, 4235, doi:10.1063/1.873159.
Parker, E. N. (1963), *Interplanetary Dynamical Processes*, chap. XIV, Wiley-Interscience, New York.
Parker, E. N. (1964), Dynamical properties of stellar coronas and stellar winds. III. The dynamics of coronal streamers, *Astrophys. J.*, *139*, 690, doi:10.1086/147795.
Pizzo, V. (1978), A three-dimensional model of corotating streams in the solar wind: 1. Theoretical foundations, *J. Geophys. Res.*, *83*, 5563, doi:10.1029/JA083iA12p05563.
Podesta, J. J. (2010), Theory of solar wind turbulence with scale-dependent alignment, anisotropy, and cross-helicity, *AIP Conf. Proc.*, *1216*, 115.
Podesta, J. J., and A. Bhattacharjee (2010), Theory of incompressible magnetohydrodynamic turbulence with scale-dependent alignment and cross-helicity, *Astrophys. J.*, *718*, 1151.
Podesta, J. J., D. A. Roberts, and M. L. Goldstein (2006), Power spectrum of small-scale turbulent velocity fluctuations in the solar wind, *J. Geophys. Res.*, *111*, A10109, doi:10.1029/2006JA011834.
Podesta, J. J., A. Bhattacharjee, B. D. G. Chandran, M. L. Goldstein, and D. A. Roberts (2008), Scale dependent alignment between velocity and magnetic field fluctuations in the solar wind and comparisons to Boldyrev's phenomenological theory, *AIP Conf. Proc.*, *1039*, 81.
Podesta, J. J., B. D. G. Chandran, A. Bhattacharjee, D. A. Roberts, and M. L. Goldstein (2009), Scale-dependent angle of alignment between velocity and magnetic field fluctuations in solar-wind turbulence, *J. Geophys. Res.*, *114*, A01107, doi:10.1029/2008JA013504.
Pope, S. B. (2000), *Turbulent Flows*, sect. 5.3, Cambridge Univ. Press, New York.
Pouquet, A., U. Frisch, and J. Leorat (1976), Strong MHD helical turbulence and the nonlinear dynamo effect, *J. Fluid Mech.*, *77*, 321, doi:10.1017/S0022112076002140.
Rajagopalan, S., C. S. Subramanian, R. A. Antonia, and A. J. Chambers (1982), Spanwise correlation of temperature in a turbulent boundary layer, *Phys. Fluids*, *25*, 1144, doi:10.1063/1.863870.
Richardson, I. G. (2006), The formation of CIRs at stream-stream interfaces and resultant geomagnetic activity, in *Recurrent Magnetic Storms: Corotating Solar Wind Streams*, *Geophys. Monogr. Ser.*, vol. 167, edited by B. Tsurutani et al., p. 45, AGU, Washington, D.C.
Richardson, I. G., and H. V. Cane (1995), Regions of abnormally low proton temperature in the solar wind (1965–1991) and their association with ejecta, *J. Geophys. Res.*, *100*, 23,397, doi:10.1029/95JA02684.
Richardson, J. D., and K. I. Paularena (2001), Plasma and magnetic field correlations in the solar wind, *J. Geophys. Res.*, *106*, 239, doi:10.1029/2000JA000071.
Richter, A. K., and A. H. Luttrell (1986), Superposed epoch analysis of corotating interaction regions at 0.3 and 1.0 AU: A comparative study, *J. Geophys. Res.*, *91*, 5873, doi:10.1029/JA091iA05p05873.
Riley, P., and J. T. Gosling (2007), On the origin of near-radial magnetic fields in the heliosphere: Numerical simulations, *J. Geophys. Res.*, *112*, A06115, doi:10.1029/2006JA012210.
Roberts, D. A. (2007), The evolution of the spectrum of velocity fluctuations in the solar wind, *Eos Trans. AGU*, *99*(52), Fall Meet. Suppl., Abstract SH31B–06.
Roberts, D. A., and S. Ghosh (1999), A kinematic analysis of the role of velocity shear in expanding plasmas, *J. Geophys. Res.*, *104*, 22,395, doi:10.1029/1999JA900272.
Roberts, D. A., L. W. Klein, M. L. Goldstein, and W. H. Matthaeus (1987a), Nature and evolution of magnetohydrodynamic fluctuations in the solar wind: Helios observations and Helios-Voyager comparisons, *J. Geophys. Res.*, *92*, 12,023, doi:10.1029/JA092iA11p12023.
Roberts, D. A., M. L. Goldstein, L. W. Klein, and W. H. Matthaeus (1987b), Origin and evolution of fluctuations in the solar wind: Voyager observations, *J. Geophys. Res.*, *92*, 11,021, doi:10.1029/JA092iA10p11021.
Roberts, D. A., M. L. Goldstein, W. H. Matthaeus, and S. Ghosh (1992), Velocity shear generation of solar wind turbulence, *J. Geophys. Res.*, *97*, 17,115, doi:10.1029/92JA01144.
Sari, J. W., and N. F. Ness (1969), Power spectra of the interplanetary magnetic field, *Sol. Phys.*, *8*, 155, doi:10.1007/BF00150667.
Schekochihin, A. A., S. C. Cowley, and W. Dorland (2007), Interplanetary and interstellar plasma turbulence, *Plasma Phys. Controlled Fusion*, *49*, A195, doi:10.1088/0741-3335/49/5A/S16.
Schlichting, H. (1979), *Boundary Layer Theory*, 7th ed., chap. 16, McGraw-Hill, New York.
Shebalin, J. V., W. H. Matthaeus, and D. Montgomery (1983), Anisotropy in MHD turbulence due to a mean magnetic field, *J. Plasma Phys.*, *29*, 525, doi:10.1017/S0022377800000933.
Siscoe, G., and D. Intriligator (1993), Three views of two giant streams: Aligned observations at 1 AU, 4.6 AU, and 5.9 AU, *Geophys. Res. Lett.*, *20*, 2267, doi:10.1029/93GL02488.
Siscoe, G. L., L. Davis, P. J. Coleman, E. J. Smith, and D. E. Jones (1968), Power spectra and discontinuities of the interplanetary magnetic field: Mariner 4, *J. Geophys. Res.*, *73*, 61, doi:10.1029/JA073i001p00061.
Siscoe, G. L., B. Goldstein, and A. J. Lazarus (1969), An east-west asymmetry in the solar wind velocity, *J. Geophys. Res.*, *74*, 1759, doi:10.1029/JA074i007p01759.
Skoug, R. M., W. C. Feldman, J. T. Gosling, D. J. McComas, and C. W. Smith (2000), Solar wind electron characteristics inside and outside coronal mass ejections, *J. Geophys. Res.*, *105*, 23,069, doi:10.1029/2000JA000017.
Smith, C. W. (2003), Magnetic helicity in the solar wind, *Adv. Space Res.*, *32*, 1971.
Smith, C. W., M. H. Acuna, L. F. Burlaga, J. L'Heureux, N. F. Ness, and J. Scheifele (1998), The ACE Magnetic Fields Experiment, *Space Sci. Rev.*, *86*, 613, doi:10.1023/A:1005092216668.

Smith, C. W., W. H. Matthaeus, G. P. Zank, N. F. Ness, S. Oughton, and J. D. Richardson (2001), Heating of the low-latitude solar wind by dissipation of turbulent magnetic fluctuations, *J. Geophys. Res.*, *106*, 8253, doi:10.1029/2000JA000366.

Smits, A. J., E. F. Spina, A. E. Alving, R. W. Smith, E. M. Fernando, and J. F. Donovan (1989), A comparison of the turbulence structure of subsonic and supersonic boundary layers, *Phys. Fluids A*, *1*, 1865.

Spangler, S. R., and L. G. Spitler (2004), An empirical investigation of compressibility in MHD turbulence, *Phys. Plasmas*, *11*, 1969.

Stanley, S. A., S. Sarkar, and J. P. Mellado (2002), A study of the flow-field evolution and mixing in a planar turbulent jet using direct numerical simulation, *J. Fluid Mech.*, *450*, 377, doi:10.1017/S0022112001006644.

Stawarz, J. E., C. W. Smith, B. J. Vasquez, M. A. Forman, and B. T. MacBride (2009), The turbulent cascade and proton heating in the solar wind at 1 AU, *Astrophys. J.*, *697*, 1119, doi:10.1088/0004-637X/697/2/1119.

Tennekes, H., and J. L. Lumley (1972), *A First Course in Turbulence*, MIT Press, Cambridge, Mass.

Thieme, K. M., E. Marsch, and R. Schwenn (1988), Relationship between structures in the solar wind and their source regions in the corona, in *Proceedings of the Sixth International Solar Wind Conference*, vol. *1*, edited by V. J. Pizzo, T. Holzer, and D. G. Sime, *NCAR Tech. Note*, *NCAR/TN-306+Proc*, 317.

Thieme, K. M., R. Schwenn, and E. Marsch (1989), Are structures in high-speed streams signatures of coronal fine structures?, *Adv. Space Res.*, *9*(4), 127, doi:10.1016/0273-1177(89)90105-1.

Thieme, K. M., E. Marsch, and R. Schwenn (1990), Spatial structures in high-speed streams as signatures of fine structures in coronal holes, *Ann. Geophys.*, *8*, 713.

Tsukahara, T., H. Kawamura, and K. Shingai (2006), DNS of turbulent Couette flow with emphasis on the large-scale structure in the core region, *J. Turbulence*, *7*, 19.

Tsurutani, B. T., and C. M. Ho (1999), A review of discontinuities and Alfven waves in interplanetary space: Ulysses results, *Rev. Geophys.*, *37*, 517, doi:10.1029/1999RG900010.

Tsurutani, B. T., C. M. Ho, E. J. Smith, M. Neugebauer, B. E. Goldstein, J. S. Mok, J. K. Arballo, A. Balogh, D. J. Southwood, and W. C. Feldman (1994), The relationship between interplanetary discontinuities and Alfven waves: Ulysses observations, *Geophys. Res. Lett.*, *21*, 2267, doi:10.1029/94GL02194.

Tsurutani, B. T., C. M. Ho, J. K. Arballo, B. E. Goldstein, and A. Balogh (1995), Large amplitude IMF fluctuations in corotating interaction regions: Ulysses at midlatitudes, *Geophys. Res. Lett.*, *22*, 3397, doi:10.1029/95GL03179.

Tu, C.-Y., and E. Marsch (1990), Evidence for a "background" spectrum of solar wind turbulence in the inner heliosphere, *J. Geophys. Res.*, *95*, 4337, doi:10.1029/JA095iA04p04337.

Tu, C.-Y., and E. Marsch (1993), A model of solar wind fluctuations with two components: Alfven waves and convective structures, *J. Geophys. Res.*, *98*, 1257, doi:10.1029/92JA01947.

Tu, C.-Y., and E. Marsch (1995a), MHD structures, waves and turbulence in the solar wind, *Space Sci. Rev.*, *73*, 1, doi:10.1007/BF00748891.

Tu, C.-Y., and E. Marsch (1995b), Comment on "Evolution of energy containing turbulent eddies in the solar wind" by W. H. Matthaeus, S. Oughton, D. H. Pontius Jr., and Y. Zhou, *J. Geophys. Res.*, *100*, 12,323, doi:10.1029/95JA01103.

Tu, C.-Y., E. Marsch, and H. Rosenbauer (1990), The dependence of MHD turbulence spectra on the inner solar wind stream structure near solar minimum, *Geophys. Res. Lett.*, *17*, 283, doi:10.1029/GL017i003p00283.

Ueno, K., K. Saito, and S. Kamiyama (2001), Three-dimensional simulation of MHD flow with turbulence, *JSME Int. J., Ser. B*, *44*, 38, doi:10.1299/jsmeb.44.38.

Vaezi, V., E. S. Oh, and R. C. Aldredge (1997), High-intensity turbulence measurements in a Taylor-Couette flow reactor, *Exp. Therm. Fluid Sci.*, *15*, 424, doi:10.1016/S0894-1777(97)00026-5.

VanZeeland, M., W. Gekelman, S. Vincena, and G. Dimonte (2001), Production of Alfven waves by a rapidly expanding dense plasma, *Phys. Rev. Lett.*, *87*, 105001, doi:10.1103/PhysRevLett.87.105001.

Veltri, P. (1994), Low frequency turbulence and energy dissipation in the solar wind, *Space Sci. Rev.*, *68*, 63, doi:10.1007/BF00749117.

Vincena, S., W. Gekelman, and J. Maggs (2004), Shear Alfven wave perpendicular propagation from the kinetic to the inertial regime, *Phys. Rev. Lett.*, *93*, 105003, doi:10.1103/PhysRevLett.93.105003.

Wu, X., and P. Moin (2008), A direct numerical simulation study on the mean velocity characteristics in turbulent pipe flow, *J. Fluid Mech.*, *608*, 81, doi:10.1017/S0022112008002085.

Yoshizawa, A., and N. Yokoi (1996), Stationary large-scale magnetic fields generated by turbulent motion in a spherical region, *Phys. Plasmas*, *3*, 3604, doi:10.1063/1.871952.

Zank, G. P., and W. H. Matthaeus (1993), Nearly incompressible fluids. II: Magnetohydrodynamics, turbulence, and waves, *Phys. Fluids A*, *5*, 257, doi:10.1063/1.858780.

J. E. Borovsky, Los Alamos National Laboratory, Mail Stop D466, Los Alamos, NM 87545, USA. (jborovsky@lanl.gov)

M. H. Denton, Department of Physics, Lancaster University, Lancaster LA1 4YW, UK.